Article

# Structure and flexibility in cortical representations of odour space

https://doi.org/10.1038/s41586-020-2451-1

Received: 7 August 2018

Accepted: 2 April 2020

Published online: 1 July 2020

Check for updates

Stan L. Pashkovski[1], Giuliano Iurilli[1,2], David Brann[1], Daniel Chicharro[1,3], Kristen Drummey[1], Kevin Franks[4], Stefano Panzeri[3] & Sandeep Robert Datta[1]✉

The cortex organizes sensory information to enable discrimination and generalization[1–4]. As systematic representations of chemical odour space have not yet been described in the olfactory cortex, it remains unclear how odour relationships are encoded to place chemically distinct but similar odours, such as lemon and orange, into perceptual categories, such as citrus[5–7]. Here, by combining chemoinformatics and multiphoton imaging in the mouse, we show that both the piriform cortex and its sensory inputs from the olfactory bulb represent chemical odour relationships through correlated patterns of activity. However, cortical odour codes differ from those in the bulb: cortex more strongly clusters together representations for related odours, selectively rewrites pairwise odour relationships, and better matches odour perception. The bulb-to-cortex transformation depends on the associative network originating within the piriform cortex, and can be reshaped by passive odour experience. Thus, cortex actively builds a structured representation of chemical odour space that highlights odour relationships; this representation is similar across individuals but remains plastic, suggesting a means through which the olfactory system can assign related odour cues to common and yet personalized percepts.

In olfaction, perception depends on chemistry[8]. Chemically related odours evoke similar percepts within and across individuals, suggesting that the cortex harbours a conserved mapping from chemical to neural space that organizes information about odour relationships to ultimately support perception[6,7]. Odours are detected by broadly tuned receptors expressed by olfactory sensory neurons, the axons of which project to the olfactory bulb (OB)[9,10]. Within the mouse OB, these axons are organized into thousands of discrete and spatially organized information channels known as glomeruli, each of which represents the tuning properties of an individual odour receptor[11]. Odour information is reformatted by OB circuits before being transmitted to cortex; it is not clear whether or to what degree this peripheral transformation preserves information about odour chemical relationships[12–14].

The main recipient of OB afferents is the piriform cortex (PCx)[1]; axons from OB projection neurons are broadly dispersed across the entire surface of the PCx, and individual PCx neurons respond to multiple, chemically distinct odorants[15–17]. These observations suggest that neurons in the PCx randomly sample sensory inputs from the OB[18,19]. Consistent with this possibility, individual odours activate ensembles of spatially distributed PCx neurons that lack apparent topographical organization with respect to chemical space[18,20,21]. Feed-forward random network models (which posit stochastic connectivity between OB glomeruli and PCx neurons) predict that PCx odour representations should be pervasively decorrelated, but that PCx should maintain the pairwise odour relationships present in the OB; these models further suggest that cortical codes for odour relationships should be invariant across individuals, as peripheral representations of chemical relationships are largely determined by the tuning properties of odour receptors, which are encoded in the genome[19,22–24].

However, in addition to receiving inputs from the OB, PCx neurons are linked through a dense web of excitatory interconnections, which suggests that the olfactory cortex acts as an auto-associative network[1,25]. Such networks use Hebbian mechanisms to construct cell assemblies that encode information about stimulus relationships (such as feature similarity or temporal coincidence) through correlated activity. In the case of PCx, auto-associative mechanisms are predicted to both increase generalization across chemically similar odours, and to render cortical odour representations sensitive to passive odour experience, thereby reshaping pairwise odour relationships inherited from OB inputs. Although the PCx exhibits characteristics that are consistent with both random and auto-associative networks, it remains unclear whether the cortex systematically encodes information about odour chemical relationships; whether any such representation preserves or reshapes odour relational information conveyed by the OB; or whether cortical odour representations are primarily decorrelated (thereby favouring odour discrimination as predicted by random network models) or correlated (thereby favouring odour generalization as predicted by auto-associative models).

## Cortex encodes odour chemical relationships

To address these questions, we used multiphoton microscopy in mice expressing the fluorescent $Ca^{2+}$ indicator GCaMP6s within the PCx to assess neural activity both in the input-dominated PCx layer 2 (L2), and

[1]Department of Neurobiology, Harvard Medical School, Boston, MA, USA. [2]Center for Neuroscience and Cognitive Systems, Istituto Italiano di Tecnologia, Rovereto, Italy. [3]Neural Computation Laboratory, Istituto Italiano di Tecnologia, Rovereto, Italy. [4]Department of Neurobiology, Duke University, Durham, NC, USA. ✉e-mail: srdatta@hms.harvard.edu

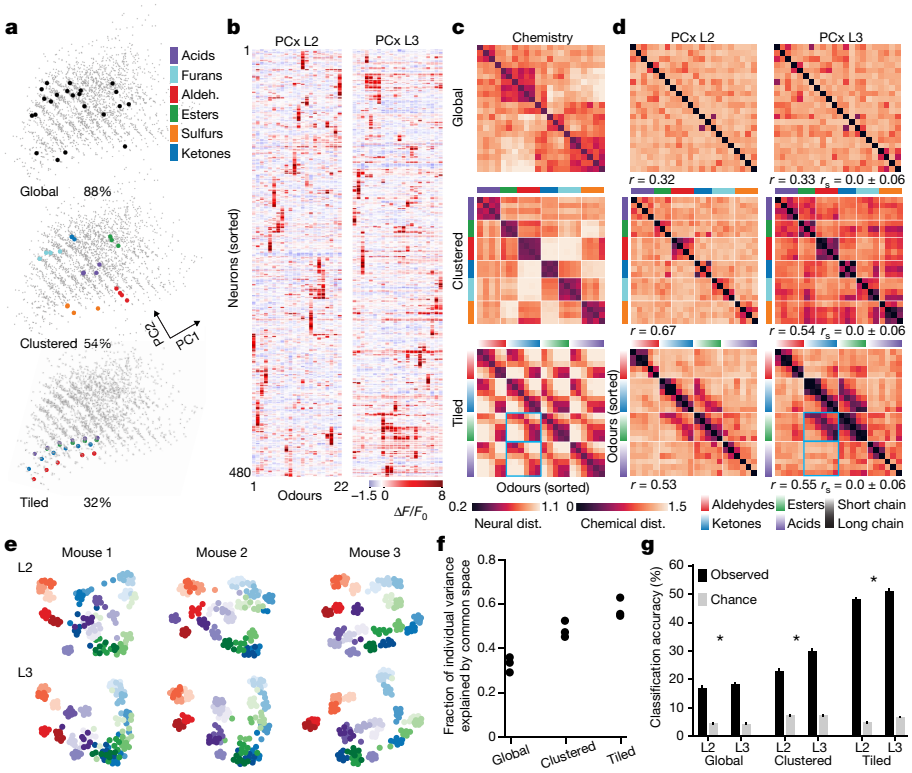


**Fig. 1 | Systematically probing relationships between odour chemistry and cortical odour representations. a**, Global, clustered and tiled odour sets (see Extended Data Fig. 1e for odour identities and structures), depicted in principal component space (see Methods). Colour indicates functional group associated with each odour. The amount of variance spanned by each odour set (of the full odour space, grey dots) is indicated. **b**, Example single neuron responses for the clustered odour set, representing the trial-averaged response of single neurons (rows) across 22 odours (columns). Rows are sorted using hierarchical clustering, with PCx L2 and L3 rasters sorted independently (Methods). **c**, Pairwise odour distances (Pearson's correlation) for all odour sets based on chemical descriptors (Methods). Rows and columns represent individual odours sorted using hierarchical clustering (ordering as in Extended Data Fig. 1e). Colour bars indicate functional groups associated with each odour. **d**, Pairwise odour distances based on pooled neural population responses in PCx L2 and L3 (Methods), sorted as in **c**. Pearson's correlation coefficient between the chemical and neural distance matrices reported below each matrix (global: $P<10^{-7}$; clustered: $P<10^{-16}$; tiled: $P<10^{-18}$); $r_s$ (shuffle) obtained by independently permuting odour labels for each neuron. Blue boxes highlight ketone-ester and ketone-acid relationships between chemistry and PCx L3. **e**, UMAP embeddings of cortical responses to the tiled odour set. Each dot represents a population response for one odour presentation (7 per odour), colour-coded as in **d**. **f**, Fraction of total variance in each mouse (L3 activity) attributable to shared across-mouse structure determined by distance covariance analysis (Methods). **g**, *k*-nearest-neighbour classification of odour identity in a held-out mouse using odour distances from other mice. Data are bootstrap mean ± s.e.m.; grey bars indicate shuffle control on odour labels (Methods). (Accuracy is greater in PCx. global: $P<10^{-3}$; clustered: $P<10^{-60}$; tiled: $P<10^{-22}$, two-sided Wilcoxon rank sum test.) Data in **b**, **d**–**g** are based on all responsive neurons (Methods) pooled by layer across mice (*n* mice, neurons (L2/L3) for global: 3, (854/616), clustered: 3, (867/488), tiled: 3, (427/334)) (see Methods for subject-specific statistics).

in the more associational layer 3 (L3, in which odour responses have not yet been described)[26] (Extended Data Fig. 1). We took advantage of a library of odour descriptors that quantifies thousands of physiochemical features, such as molecular weight, polarizability and hydrophobicity[5,27], to rationally design three sets of 22 odours each: a 'global' odour set, which included structurally diverse odorants well separated in odour space; a 'clustered' odour set divided into six odour subsets, each of which shared functional groups and other structural features; and a 'tiled' odour set, in which the carbon chain length of a ketone, an ester, an aldehyde and an acid was incrementally varied (Fig. 1a, Extended Data Fig. 1, Methods). Although each odour set captured progressively less chemical variance, by construction individual odours in the clustered set (within each of the six subsets) were most closely related, whereas odours were separated at intermediate distance scales in the tiled set. We noted that under anaesthesia odour responses in L3 (and to a lesser extent L2) were attenuated or absent; recordings were therefore performed during wakefulness, a state in which L3 neurons were considerably more active (Extended Data Fig. 2, Methods).

All odours evoked selective excitation and suppression, with PCx L3 responses being denser, broader and more reliable than those in L2 (Extended Data Fig. 3). Odours evoked more correlated activity across the population of PCx neurons (that is, ensemble correlations) than was expected by chance, with greater correlations observed in L3 compared to L2 (Fig. 1b, Extended Data Fig. 3). These findings raised the possibility that correlated odour-evoked responses among PCx ensembles systematically reflect chemical relationships among odour stimuli. To explore this possibility, correlation distance matrices were generated for each odour set based on the physiochemical descriptors that characterize each odorant (Fig. 1c, Methods). Odours in the global set were the least chemically correlated with each other, whereas odours in the clustered odour set exhibited substantial block diagonal structure, consistent with subsets of odours sharing key chemical attributes. Because molecules in the tiled set are related along two chemical axes (for example, heptanone and octanone differ by one carbon atom, whereas heptanone and pentyl acetate differ by one oxygen atom), the matrix describing these odours exhibited periodic on- and off-diagonal structure.

Visual comparison and quantification demonstrated that odour chemistry and neural responses were only weakly related in the global odour set; by contrast, cortical odour responses maintained the block

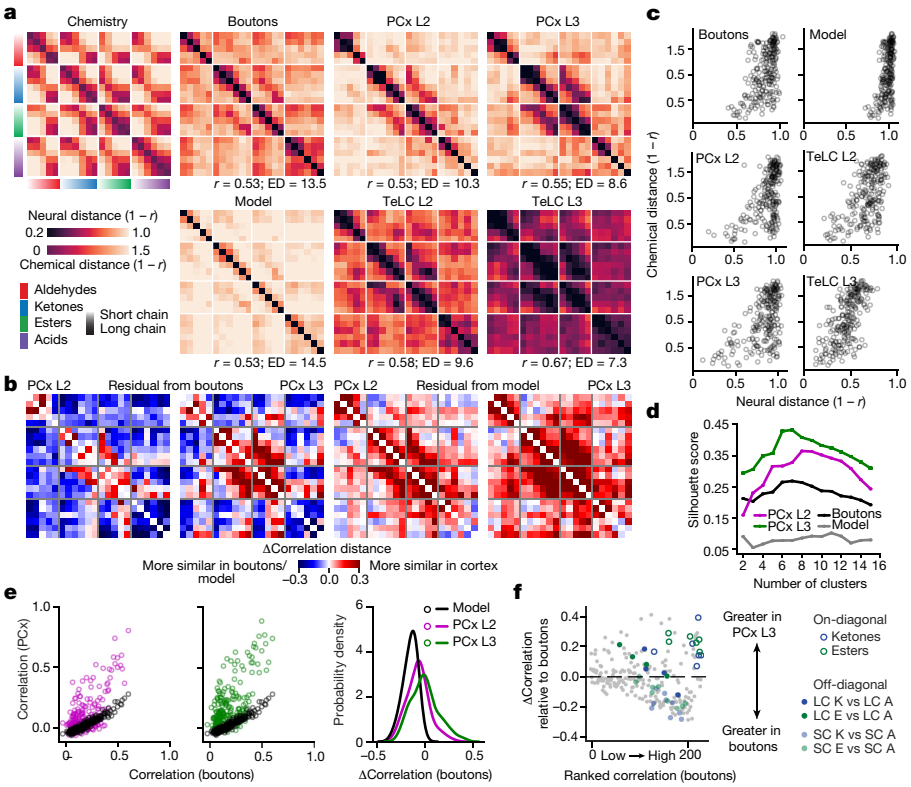


**Fig. 2 | Correlation structure differs in olfactory bulb and cortex. a**, Correlation distance matrices for the tiled odour set across all conditions. Top left, distances obtained using chemical descriptors. Right, distances based on odour responses. Odour sorting as in Fig. 1c. *r* values indicate Pearson's correlation with odour chemistry (Boutons: $P < 10^{-17}$; PCx L2: $P < 10^{-17}$; PCx L3: $P < 10^{-19}$; Model: $P < 10^{-17}$; TeLC L2: $P < 10^{-21}$; TeLC L3: $P < 10^{-32}$; shuffled Pearson's $r = 0.0 \pm 0.063$ (mean ± s.d.), 1,000 permutations on odour label). ED, effective dimensionality (Methods). **b**, Left, difference between PCx and bouton distances in **a**. Right, difference between PCx and random network model distances in **a** (Methods). **c**, Pairwise odour correlation distances based on neural responses plotted against corresponding chemical distances. **d**, Silhouette scores for clustered population responses (based upon Euclidean distances and grouped via *k*-means clustering) over a range of cluster sizes. Higher values indicate better clustering (Methods). **e**, Left, pairwise odour correlations in boutons and PCx predicted by the feed-forward random network model (Methods) compared to observed correlations in PCx L2 and L3. Right, probability density distribution of differences between cortical (PCx L2 and L3) and input (boutons) pairwise odour correlations, superimposed on the distribution expected with the model (model versus L3: $P < 10^{-33}$, versus L2: $P < 10^{-17}$, Kolmogorov–Smirnov test). **f**, Difference in pairwise odour correlations between PCx L3 and boutons (grey dots). Positive values indicate greater correlation in the cortex. Odour pairs are ranked along the *x* axis from least to highest correlation in the bouton data. Short-chain (SC) and long-chain (LC) comparisons between ketones (K), esters (E) and aldehydes (A) are colour-coded as shown.

diagonal physiochemical correlation structure apparent in the clustered odour set, demonstrating that at close chemical distances, PCx represents odour chemical relationships (Fig. 1d). Notably, neural responses to the tiled odour set (in which odour relationships are organized at intermediate chemical distances) reflected on-diagonal chemical relationships, but did not uniformly encode off-diagonal relationships. For example, the cortex appeared to emphasize chemical similarities between ketones and esters, while de-emphasizing chemical similarities between ketones and acids (Fig. 1d, highlighted blue boxes). Structured chemical–neural relationships were apparent on a trial-by-trial basis, and persisted for several seconds after odour offset; as has been observed previously under anaesthesia, no spatial ordering of neurons was observed with respect to odour chemistry during wakefulness, consistent with response correlations alone conveying information about odour relationships[18,20] (Extended Data Fig. 4).

Both uniform manifold approximation and projection (UMAP) embeddings and manifold alignment revealed that cortical odour relationships were similar across mice (Fig. 1e, f); indeed, information about pairwise cortical odour distances derived from one mouse could be used to predict the identity of a held-out odorant based upon odour distances measured in a different mouse, with better performance observed in L3 than L2 (Fig. 1g, Methods). Lasso optimization was used to identify chemical features relevant to driving neural responses in each of the odour sets; identified descriptors captured physiochemical features such as molecular weight, electronegativity, polarizability and hydrophobicity, which suggests that ensemble-level odour representations are driven by diverse aspects of odour chemistry (Supplementary Table 1, Methods). Identified features that predicted neural activity for each odour set also improved the correspondence between all the other odour sets and their associated neural activity, demonstrating that information about odour chemistry gleaned from one experiment can be used to predict cortical responses in a different experiment carried out using a separate set of odorants (Extended Data Fig. 5a).

## Cortical odour representations reshape bulb inputs

The selective differences between odour chemical relationships and cortical activity apparent in the tiled odour experiment could reflect correlation structure present in OB inputs to PCx (consistent with feed-forward random network models), or instead could be generated by cortex (consistent with auto-associative models). However, until now it has not been possible to quantify odour-evoked responses across the complete array of OB glomeruli, which has prevented the characterization of correlation structure in bulb inputs to PCx. To

address this challenge, we introduced synaptically targeted GCaMP6s into projection neurons spanning the OB, and imaged odour evoked activity in boutons in PCx layer 1a (L1a), where they synapse with L2 and L3 neurons; because the axons and boutons of all OB glomeruli are spatially distributed across the PCx[15,16], each cortical field of view effectively samples glomeruli from the entire bulb (Methods, Extended Data Fig. 6).

Odours from the tiled odour set evoked both excitation and suppression in OB boutons, the responses of which were similar across mice (Extended Data Fig. 7). Correlation distance matrices revealed that bouton responses reflected information about odour chemical relationships (Fig. 2a); in addition, identification of physiochemical features that optimized the observed chemical-bouton relationships improved predictions of bouton responses to held-out odours as well as predictions of cortical responses to the tiled odour set (Extended Data Fig. 5b, Supplementary Table 1). Thus, similar to the cortex, OB projection neuron boutons encode information about odour relationships and chemistry.

However, odour responses in boutons and cortex exhibited distinct patterns of correlation with respect to chemistry, with the greatest chemical–neural differences observed in PCx L3 (Fig. 2a, b). Although the average level of correlated activity was similar in boutons and cortex, the distribution of odour-evoked correlations differed, with bouton representations exhibiting higher effective dimensionality (see Methods); by contrast, odour responses of PCx L3 neurons were more clustered, more selectively structured, and exhibited both lower effective dimensionality and a wider dynamic range for representing close chemical relationships (Fig. 2a, c–e, Extended Data Fig. 7). The presence of these structured correlations in part reflected increased grouping of closely related odorants, as representations for odours nearest each other in chemical space (that is, on-diagonal correlation matrix relationships) were more clustered in the cortex than in boutons (Fig. 2a, f). One exception to this trend was acids, which as a class were correlated in the OB but relatively decorrelated in the cortex (Fig. 2a).

Odour relationships were also reshaped in the cortex compared to those in odour chemistry and boutons. UMAP embeddings of data from the tiled odour experiment (in which chain length and functional group are the main axes of chemical variation) suggested that boutons largely organize odour information along a single axis that emphasizes chain length (again, with the exception of acids) (Methods); by contrast, odour information in PCx L3 appeared largely organized in two dimensions based on functional group (Fig. 3a). Similar functional group-based reorganization was observed via hierarchical clustering (Fig. 3b). Lasso optimization confirmed that boutons and cortex differentially weight chemical features related to chain length and functional group (Extended Data Fig. 5c).

Moreover, several pairwise odour relationships were reorganized in PCx on the basis of both chain length and function group. For example, in chemical space, short-chain and long-chain odours with different functional groups were similarly cross-correlated; in boutons, correlations between short-chain aldehydes and esters were emphasized whereas those among long-chains were diminished; and in PCx L3, the opposite pattern was observed, with long-chain aldehydes and esters exhibiting stronger correlations and short-chains exhibiting weaker correlations (Fig. 3c). Chain-length-dependent cortical reshaping of odour relationships was also apparent between aldehydes and ketones.

These differences in correlation structure suggest that PCx and OB boutons differentially encode information about odour identity and odour relationships. Linear decoders based on cortical responses (particularly from PCx L3) were worse than OB-based decoders at predicting odour identity on each trial, consistent with bouton odour responses having a higher dimensionality (Fig. 4a). By contrast, cortex (particularly PCx L3) was on average better at encoding information about odour relationships (Fig. 4b); notably, however, OB was better at

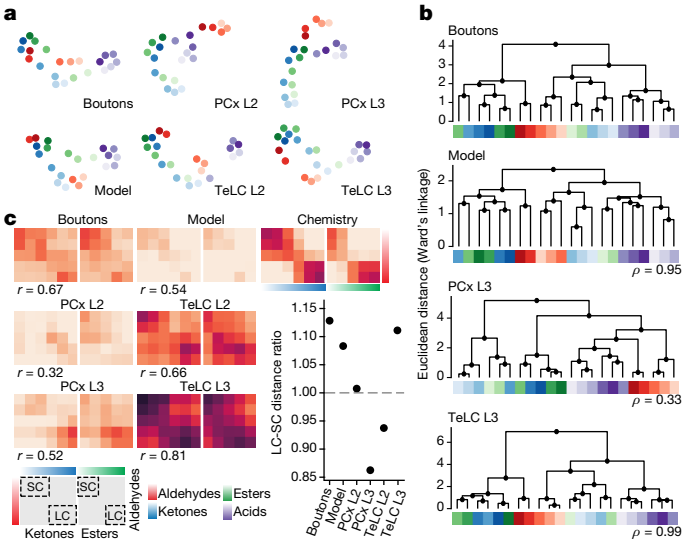


**Fig. 3 | Cortical odour responses reformat odour relationships inherited from the OB. a**, UMAP embeddings for all experimental conditions. Note that UMAP emphasizes relationships rather than distances, so these embeddings are similarly scaled; without such scaling the points in the model panel, for example, would be much more separated than those in the PCx L3 panel (Fig. 2a, Methods). **b**, Hierarchical clustering of neural population responses; $\rho$ values indicate clustering similarity to OB boutons (Spearman correlation on cophenetic distances between boutons and the other data sets). **c**, Enlarged regions from correlation matrices in Fig. 2a depicting conserved and rearranged odour relationships between aldehydes, ketones and esters; inset: ratio of correlations between long-chain and short-chain comparisons (each dot indicates mean across odour pairs); $r$ values indicate Pearson's correlation to odour chemistry. Colour code in **a** and **b** is as in **c**.

generalizing across short-chain ketones, aldehydes and esters whereas cortex was better at generalizing across the corresponding long-chains, consistent with the observed differences in correlation structure for these odour classes (Figs. 3c, 4c).

Given these differences in information content, we assessed whether bulbar or cortical odour codes more closely correspond to perceptual odour relationships by measuring the innate perceptual similarity of odour pairs through a cross-habituation assay[28] (Extended Data Fig. 8). Perceptual odour relationships better matched odour responses in PCx L3 than those in OB or PCx L2 (Fig. 4d); this closer correspondence to PCx L3 was particularly apparent for the short-chain–short-chain and long-chain–long-chain comparisons, whose pattern of neural correlation was inverted in bulb and cortex (Fig. 3c).

## OB–PCx transformation requires associative network

Together, our observations suggest that the transformation between bulb and cortex reflects the combined influence of random network-type connectivity (which maintains odour relationships) and an auto-associative mechanism (which generally clusters and can selectively reshape odour relationships). To directly assess the contribution of random network-type connectivity to the observed cortical odour responses, bouton odour responses were passed through a previously established feed-forward model in which simulated PCx neurons stochastically sample from multiple glomerular inputs[19] (Methods). Consistent with previous reports, the model predicted decorrelated cortical odour representations, whose pairwise relationships were preserved relative to boutons (Fig. 2a). Although cortical responses were in part consistent with model output—as many pairwise odour relationships were preserved—the model failed to capture the strong correlation

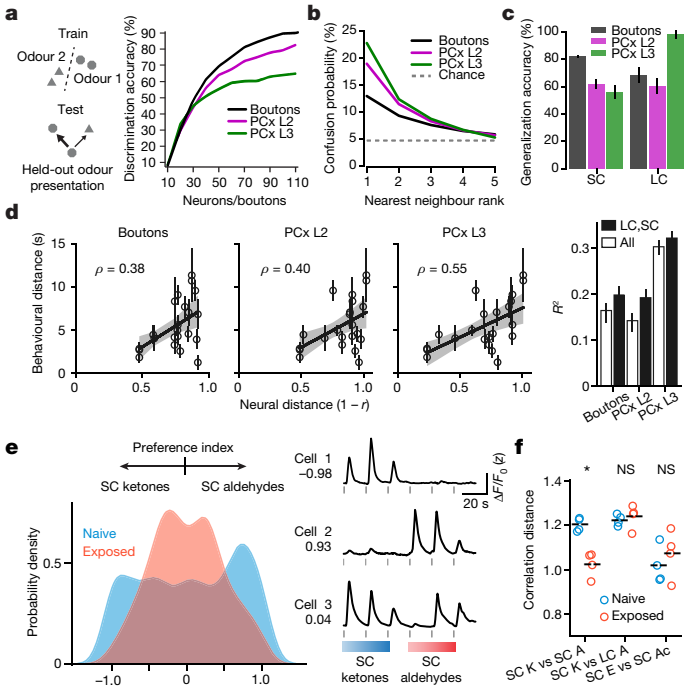


**Fig. 4 | Cortical odour representations generalize across odours, are consistent with perception, and can be modified by experience. a**, Left, schematic depicting a linear support vector machine (SVM) classifier trained to identify an odour associated with a held-out neural population response on a trial-by-trial basis. Right, decoding accuracy plotted against neural/bouton populations of different sizes. **b**, Decoding analysis to quantify odour generalization; each line represents classifier confusion between any odour and all other odours, rank ordered by the degree of confusion. **c**, Decoding accuracy of SVM classifiers predicting whether a held-out odour is a short-chain or long-chain molecule. The acid block was excluded for this analysis. Data are bootstrapped mean ± s.e.m. across held-out odours and neural/bouton ensembles. (In **a**–**c**: tiled odour set, 22 odours; number of mice, neurons/boutons for PCx L2/L3 as in Fig. 1b, d–g, for boutons, 6 mice /3,160 boutons. In **b**, **c**: 300 units, 100 bootstraps. See Methods for all decoding analyses). **d**, Left, pairwise neural and behavioural odour distances from a cross-habituation assay for the tiled odour set (Extended Data Fig. 8); $\rho$ is Spearman correlation coefficient. Black line indicates regression fit (mean ± 95% confidence interval, 1,000 bootstraps). Black circles are mean ± s.e.m across mice ($n > 3$ for each comparison). Right, coefficient of determination ($R^2$) based on short-chain–short-chain and long-chain–long-chain or all comparisons (median ± 66th confidence interval, 1,000 bootstraps. $n = 26$ odour triplets; 122 mice across all conditions, see Methods for behavioural distance and odour identities). **e**, Left, probability density estimates of cell-wise class preference index for naive and passive odour exposure conditions, for neurons responding to at least one short-chain ketone or aldehyde (Methods). Right, example $z$-scored fluorescence (and preference index) from neurons tuned to short-chain ketones (cell 1), short-chain aldehydes (cell 2), or both (cell 3). Grey bars indicate odour onset. **f**, Pairwise odour distances in PCx L3 from odour-naive and odour-exposed mice. Passive exposure to the target mixture (short-chain ketones and aldehydes) specifically increased similarity between ketones and aldehydes, but not between control odour pairs (short-chain ketones vs long-chain aldehydes and short-chain esters vs short-chain acids (Ac)) (Extended Data Fig. 10). *$P < 0.002$; NS (not significant) middle: $P = 0.62$; right: $P = 0.45$, two-tailed independent $t$-test. Number of mice/neurons for naive: 3/334; exposed: 3/742.

structure present in cortex or the selective rewriting of pairwise odour relationships (Figs. 2a–e, 3).

To evaluate the relative influence of auto-associative mechanisms on cortical odour representations, we used an adeno-associated virus (AAV)-based method to express tetanus toxin light chain (TeLC) within PCx neurons; this approach blocks synaptic transmission and causes PCx to behave as if it largely receives feed-forward inputs[29] (Extended Data Fig. 9). After attenuation of the associative network, the tuning of single neurons to odours broadened, response densities rose, and odour correlations increased, consistent with known network-dependent recruitment of inhibition[29] (Extended Data Fig. 9). Crucially, after TeLC infection, cortical odour relationships more closely resembled those present in odour chemistry and OB axonal boutons as assessed via correlation matrices, UMAP clustering and hierarchical clustering; for example, the cortical restructuring of short-chain and long-chain odour relationships was abolished, as was the decorrelation among acids (Figs. 2a–c, 3).

Auto-associative networks are predicted to influence correlations among odour representations to reflect the coincidence of stimuli in the world; although reward-based experiments have revealed task-dependent changes in cortical odour relationships[30,31], it has not yet been demonstrated that cortical odour correlations are sensitive to passive odour experience[1,25]. We therefore repeatedly exposed mice to a mixture of short-chain aldehydes and ketones (the PCx L3 representations of which are relatively decorrelated) (Fig. 2a) before assessing cortical responses to the tiled odour set. Mixture experience specifically increased the cortical correlation between individual aldehydes and ketones, and recruited single neuron tuning curves that reflected generalized responses to these specific odour classes (Fig. 4e, f, Extended Data Fig. 10). These observations demonstrate that cortical odour relationships can adapt to the statistics of the experienced odour environment.

## Discussion

The olfactory system must synthesize information about chemical features to generate organized odour representations that support discrimination and generalization. Here we show that both OB boutons and cortex explicitly represent odour chemical relationships. The observation that many pairwise odour relationships are encoded similarly in these two brain areas is consistent with random connectivity models, which propose that PCx neurons stochastically sample glomeruli to generate a systematic population-level representation of odour chemical space[19].

However, cortex differs from the bulb in two key respects. First, PCx better clusters odour representations, enabling it to preferentially signify odour relationships. Second, cortex reconfigures information about odour relationships inherited from the bulb—the cortex does not simply pool and normalize its inputs, but instead, in a network-dependent manner, actively builds an odour space to emphasize certain odour relationships and de-emphasize others; this re-writing is sensitive to odour exposure, which can recruit new single neuron tuning properties and modify odour relationships. The olfactory system, therefore, transforms a chemical feature space into a cortical space that represents stimulus relationships through correlated activity; the structure of this space reflects information inherited from the sensory periphery, the transformation imposed by cortical circuits, and the effects of sensory experience. The cortical grouping of representations for both structurally and temporally related odours suggests a mechanism for generalization across natural odour sources, which tend to emit related odour chemicals; in principle, similar mechanisms could assign coincidentally encountered but structurally distinct odours to shared semantic categories[32–34]. Future in vivo experiments will be required to understand how the intrinsic properties of PCx neurons and the associative network, which targets both excitatory pyramidal and inhibitory neurons, collaborate to transform and organize odour representations.

In nearly all our analyses, the correlation structure of L2 odour representations was intermediate between that observed in boutons and L3, which may reflect relative differences in the prominence of

bulb inputs in L2 and associational connectivity in L3[1,26]. Because the network that interconnects PCx neurons also sends centrifugal projections to the OB, it is likely that under physiological circumstances this network influences both bulb and cortical representations of odour relationships[12,29,35,36]. Although the TeLC experiment demonstrates that network activity originating in PCx is required for the bulb–cortex transformation, PCx is recurrently connected to an array of higher olfactory centres that may also have a role in shaping odour relationships[2]. Notably, neural representations in PCx L3 more closely match perception than those present in bulbar inputs, suggesting a functional hierarchy among at least some interconnected olfactory brain areas.

Relationships among cortical odour representations depend on chemical distances, such that at close distances information about chemical relationships is largely maintained, at large distances cortex decorrelates odour representations, and at the intermediate distances captured by the tiled odour set the olfactory system sculpts relational representations for odours in a manner that respects but reshapes chemical relationships. Our findings with the clustered odour set are reminiscent of previous work demonstrating that similar odour mixtures recruit overlapping ensembles of PCx neurons, although in those experiments chemical distances were not quantified[3]. Although here we take advantage of functional groups and chain lengths to systematically alter odour distances at intermediate scales, many distinct chemical features differentially contribute to odour representations in both the bulb and cortex[4]. The finding that treating odour chemicals as buckets of physiochemical features—rather than organizing information about chemistry along arbitrary dimensions—identifies structured chemical–neural–perceptual relationships is consistent with the longstanding model that the odour receptor repertoire broadly samples chemical feature space[5,10,27].

The relational information present in PCx cannot, in and of itself, assign a given odorant to its unique odour quality: the mapping observed here potentially explains why lemon characteristically smells similar to orange, but fails to explain why lemon smells like lemon. In particular, it is unclear how cortical information about odour relationships might be aligned to enable lemon odour to evoke a similar percept across individuals. We propose that relational information in PCx (and possibly other olfactory areas) is translated into invariant information about odour quality by using universal points of reference, much like a compass can be used to orient a paper map to the cardinal directions[19]. These points of reference may arise from invariant properties of specific odour receptors, or from hardwired circuits in olfactory areas such as the accessory olfactory nucleus or the cortical amygdala[15,16,37]. Alternatively, reference points could be learned from shared experience; in this model exposure to stereotyped odours (for example, amniotic fluid, mother's milk, faeces, urine or food) or common objects (such as actual lemons) could orient chemical-neural mappings along (largely) invariant axes across individuals. Further work aimed at understanding the interaction between fixed and flexible features of olfactory circuitry will be required for a full account of the relationship between chemistry, experience and perception.

## Online content

Any methods, additional references, Nature Research reporting summaries, source data, extended data, supplementary information, acknowledgements, peer review information; details of author contributions and competing interests; and statements of data and code availability are available at https://doi.org/10.1038/s41586-020-2451-1.


1. Haberly, L. B. Parallel-distributed processing in olfactory cortex: new insights from morphological and physiological analysis of neuronal circuitry. *Chem. Senses* **26**, 551–576 (2001).
2. Courtiol, E. & Wilson, D. A. The olfactory mosaic: bringing an olfactory network together for odor perception. *Perception* **46**, 320–332 (2017).
3. Barnes, D. C., Hofacer, R. D., Zaman, A. R., Rennaker, R. L. & Wilson, D. A. Olfactory perceptual stability and discrimination. *Nat. Neurosci.* **11**, 1378–1380 (2008).
4. Wilson, D. A. & Sullivan, R. M. Cortical processing of odor objects. *Neuron* **72**, 506–519 (2011).
5. Haddad, R. et al. A metric for odorant comparison. *Nat. Methods* **5**, 425–429 (2008).
6. Dravnieks, A. Odor quality: semantically generated multidimensional profiles are stable. *Science* **218**, 799–801 (1982).
7. Schiffman, S. S. Physicochemical correlates of olfactory quality. *Science* **185**, 112–117 (1974).
8. Amoore, J. E. Stereochemical theory of olfaction. *Nature* **198**, 271–272 (1963).
9. Buck, L. & Axel, R. A novel multigene family may encode odorant receptors: a molecular basis for odor recognition. *Cell* **65**, 175–187 (1991).
10. Malnic, B., Hirono, J., Sato, T. & Buck, L. B. Combinatorial receptor codes for odors. *Cell* **96**, 713–723 (1999).
11. Mombaerts, P. et al. Visualizing an olfactory sensory map. *Cell* **87**, 675–686 (1996).
12. Otazu, G. H., Chae, H., Davis, M. B. & Albeanu, D. F. Cortical feedback decorrelates olfactory bulb output in awake mice. *Neuron* **86**, 1461–1477 (2015).
13. Friedrich, R. W. & Wiechert, M. T. Neuronal circuits and computations: pattern decorrelation in the olfactory bulb. *FEBS Lett.* **588**, 2504–2513 (2014).
14. Chae, H. et al. Mosaic representations of odors in the input and output layers of the mouse olfactory bulb. *Nat. Neurosci.* **22**, 1306–1317 (2019).
15. Sosulski, D. L., Bloom, M. L., Cutforth, T., Axel, R. & Datta, S. R. Distinct representations of olfactory information in different cortical centres. *Nature* **472**, 213–216 (2011).
16. Miyamichi, K. et al. Cortical representations of olfactory input by trans-synaptic tracing. *Nature* **472**, 191–196 (2011).
17. Davison, I. G. & Ehlers, M. D. Neural circuit mechanisms for pattern detection and feature combination in olfactory cortex. *Neuron* **70**, 82–94 (2011).
18. Stettler, D. D. & Axel, R. Representations of odor in the piriform cortex. *Neuron* **63**, 854–864 (2009).
19. Schaffer, E. S. et al. Odor perception on the two sides of the brain: consistency despite randomness. *Neuron* **98**, 736–742.e3 (2018).
20. Roland, B., Deneux, T., Franks, K. M., Bathellier, B. & Fleischmann, A. Odor identity coding by distributed ensembles of neurons in the mouse olfactory cortex. *eLife* **6**, e26337 (2017).
21. Iurilli, G. & Datta, S. R. Population coding in an innately relevant olfactory area. *Neuron* **93**, 1180–1197 (2017).
22. Babadi, B. & Sompolinsky, H. Sparseness and expansion in sensory representations. *Neuron* **83**, 1213–1226 (2014).
23. Barak, O., Rigotti, M. & Fusi, S. The sparseness of mixed selectivity neurons controls the generalization-discrimination trade-off. *J. Neurosci.* **33**, 3844–3856 (2013).
24. Dasgupta, S., Stevens, C. F. & Navlakha, S. A neural algorithm for a fundamental computing problem. *Science* **358**, 793–796 (2017).
25. Haberly, L. B. & Bower, J. M. Olfactory cortex: model circuit for study of associative memory? *Trends Neurosci.* **12**, 258–264 (1989).
26. Bekkers, J. M. & Suzuki, N. Neurons and circuits for odor processing in the piriform cortex. *Trends Neurosci.* **36**, 429–438 (2013).
27. Saito, H., Chi, Q., Zhuang, H., Matsunami, H. & Mainland, J. D. Odor coding by a Mammalian receptor repertoire. *Sci. Signal.* **2**, ra9 (2009).
28. Cleland, T. A., Morse, A., Yue, E. L. & Linster, C. Behavioral models of odor similarity. *Behav. Neurosci.* **116**, 222–231 (2002).
29. Bolding, K. A. & Franks, K. M. Recurrent cortical circuits implement concentration-invariant odor coding. *Science* **361**, eaat6904 (2018).
30. Chapuis, J. & Wilson, D. A. Bidirectional plasticity of cortical pattern recognition and behavioral sensory acuity. *Nat. Neurosci.* **15**, 155–161 (2011).
31. Shakhawat, A. M., Harley, C. W. & Yuan, Q. Arc visualization of odor objects reveals experience-dependent ensemble sharpening, separation, and merging in anterior piriform cortex in adult rat. *J. Neurosci.* **34**, 10206–10210 (2014).
32. Sell, C. S. in *Chemistry and the Sense of Smell* **Ch. 5**, 237–296 (Wiley, 2014).
33. Gottfried, J. A., Winston, J. S. & Dolan, R. J. Dissociable codes of odor quality and odorant structure in human piriform cortex. *Neuron* **49**, 467–479 (2006).
34. Fournel, A., Ferdenzi, C., Sezille, C., Rouby, C. & Bensafi, M. Multidimensional representation of odors in the human olfactory cortex. *Hum. Brain Mapp.* **37**, 2161–2172 (2016).
35. Diodato, A. et al. Molecular signatures of neural connectivity in the olfactory cortex. *Nat. Commun.* **7**, 12238 (2016).
36. Boyd, A. M., Kato, H. K., Komiyama, T. & Isaacson, J. S. Broadcasting of cortical activity to the olfactory bulb. *Cell Rep.* **10**, 1032–1039 (2015).
37. Schoenfeld, T. A. & Macrides, F. Topographic organization of connections between the main olfactory bulb and pars externa of the anterior olfactory nucleus in the hamster. *J. Comp. Neurol.* **227**, 121–135 (1984).

# Methods

### Ethical compliance

All experimental procedures were approved by the Harvard Medical School Institutional Animal Care and Use Committee (protocol number 04930) and were performed in compliance with the ethical regulations of Harvard University as well as the Guide for Animal Care and Use of Laboratory Animals.

### Mice

Acute imaging of PCx was performed in 8–16-week-old C57/BL6J (Jackson Laboratories) male mice. Imaging of cortical neurons was performed in mice harbouring the *Vgat-ires-cre* knock-in allele (Jackson Stock no. 028862) and the *ROSA26-LSL-TdTomato cre* reporter allele (Jackson Stock no. 007914); imaging of boutons was performed in mice containing the *Tbx21-cre* allele (Jackson Stock no. 024507, gift from C. Dulac). TeLC-dependent elimination of cortical excitatory transmission and subsequent imaging was performed in Emx1-IRES-Cre mice (Jackson Stock no. 005628). Male mice were group-housed before viral delivery of GCaMP6s and housed singly for 1–3 weeks after injection.

### Viral constructs

To generate pAAV-hSyn-FLEX-TeLC-P2A-dTom, pAAV-hSyn-FLEX-TeLC-P2A-EYFP (a gift from Bernardo Sabatini) was digested with AscI and NheI to remove enhanced yellow fluorescent protein (eYFP). A gene fragment (synthesized by IDT) containing dTomato with the SV40 nuclear localization signal was cloned into the TeLC backbone via isothermal assembly (NEB HIFI E2621). AAVDJ-hSyn-FLEX-TeLC-P2A-dTom virus was produced by Vigene Biosciences, with a titre of $1.5 \times 10^{13}$ genome copies per ml. AAV PHP.eB hSynapsin1-FLEx-axon-GCaMP6s virus was produced as previously described[38]. In brief, HEK293T cells were co-transfected with pAAV-hSynapsin1-FLEx-axon-GCaMP6s (a gift from L. Tian, Addgene plasmid 112010), PHP.eB rep-cap (a gift from the Viviana Gradinaru Lab/Clover centre), and adenovirus helper plasmids. After 5 days, viral particles were collected and then purified via iodixanol gradient ultracentrifugation. The virus was titred via quantitative PCR (qPCR); the titre of all batches was between $2 \times 10^{13}$–$3 \times 10^{13}$ viral genomes per ml.

### Stereotaxic viral delivery

*Vgat-ires-cre; ROSA26-LSL-TdTomato* male mice were injected with an AAV expressing the genetically encoded activity indicator GCaMP6s (AAV1.CAG.GCaMP6s.WPRE.SV40, Penn Vector Core). Injections were targeted to posterior PCx using Allen Brain Atlas coordinates: medial–lateral (ML): −4.2, anterior–posterior (AP): −1.09, dorsal–ventral (DV): −4.25, from the dura. FLEX-TeLC-P2A-dTom was targeted to anterior and posterior PCx of both hemispheres of Emx1-IRES-Cre mice at AP: 0.39 and −1.0; ML: −3.51 and −4.2; DV: −4.4 and −4.1. To uniformly infect olfactory bulb projection neurons, AAV PHP.eB FLEX-axon-GCaMP was delivered intravenously via retro-orbital injections in Tbx21-Cre transgenic mice (Jackson Stock no. 024507), which express Cre recombinase in OB projection neurons.

Full-titre viruses (500–1,000 nl) were delivered to cortex at 1 nl $s^{-1}$ using a Nanoject II dispensing pump (Drummond Scientific). GCaMP6s-injected mice were imaged 1–3 weeks after delivery. In TeLC experiments, GCaMP6s was injected at ML: −4.2, AP: −1.09, DV: −4.25, from the dura, 2–3 weeks after TeLC delivery. Mice were imaged 3–5 weeks after TeLC delivery. Imaging of OB projection neuron axon terminals in L1a of PCx was performed 3–5 weeks after retro-orbital injection. To assess the influence of passive odour exposure on cortical representations (see 'Passive odour exposure'), odour exposure to mixtures was initiated 1–2 weeks after viral delivery; as with imaging in odour-naive mice, imaging in odour-exposed mice was performed 3–4 weeks after injection.

Uniform infection of L2 and L3 cortical neurons by AAV-TeLC across the rostro-caudal extent of PCx was confirmed histologically. To validate TeLC dependent inhibition of cortical excitatory synaptic transmission, odour-evoked single-unit activity was compared between control and infected mice as previously described[29].

### Surgical approach and craniotomy

We developed a surgical preparation compatible with PCx imaging during wakefulness and semi-paralysis; this preparation is similar to those used in the past to explore in vivo neural responses without the use of general anaesthesia (but with effective analgesia) during the experiment[39–41]. Before exposing PCx, mice were anaesthetized with isoflurane, and head-fixed with dental cement to a rotating headpost. The PCx was then accessed from the ventral surface of the mouse skull through surgical resection of the zygoma, the mandible, and associated musculature and fascia. A 2 mm craniotomy overlying the PCx was made using a dental drill and secured with a custom-shaped cranial window.

To ensure that the mouse was free of pain and discomfort during wakefulness and semi-paralysis, full hemifacial analgesia was provided by performing a complete trigeminal nerve block. This procedure is designed to abolish sensation around the surgical exposure, as well as the ipsilateral oro-facial region encompassing the entire dorsoventral extent of the head and extending from the nostril to the neck. The junction of the four branches of the trigeminal ganglion was readily identified at the external pterygoid ridge, which was rendered accessible when the mandible was removed. A 1–5 µl, 0.2–1.0 mg $kg^{-1}$ dose of bupivacaine was injected directly into the stalk of the trigeminal nerve bundle using a calibrated micropipette mounted on a micro-manipulator. By infusing bupivacaine solution proximally to the trigeminal ganglion, distribution along all trigeminal branches, including the mandibular, ophthalmic, and infraorbital branches, was ensured. To verify that the block infiltrated the entire nerve bundle, each injection was supplemented with the fluorescent lipophilic contrast agent DiI used to identify myelinated nerve fibres, owing to its lipophilic, infiltrating nature[42]. By including DiI in the block solution and monitoring its diffusion through the nerve adjacent to the injection site, proper micropipette placement directly inside the nerve bundle was confirmed. Successful DiI injections were characterized by uniform distribution of dye through the trigeminal bundle proximal to the injection site. In cases of insufficient labelling of the nerve bundle, several injections were administered until the entire nerve was labelled by visual inspection. This procedure was extensively evaluated through measurements of heart rate (which revealed no signs of distress)[43] (Extended Data Fig. 2) and by systematically probing the depth of analgesia through the use of needle pricks along the entire dorso-ventral and rostro-caudal portion of the head ipsilateral to the injection site.

After completion of the surgical exposure, induction of analgesia, installation of paralytic infusion and retro-nasal sniffing lines, as well as placement of the EEG electrode (see 'Semi-paralysis', 'Artificial sniffing' and 'EEG for assessing brain state' sections), isoflurane anaesthesia was discontinued and mice were transferred to the imaging set-up equipped with custom-built sniff generator, oxygen respirator, as well as a peristaltic pump for paralytic infusion.

### Semi-paralysis

Mice were provided with a continuous infusion of a low dose of the muscle relaxant pancuronium bromide into the jugular vein during the imaging phase of the experiment[40]. After calibration, the final dose and infusion speeds were chosen to be 0.024 ng $kg^{-1}$ per 10 min. At this dose, mice experience a loss of righting reflex, but maintain diaphragmatic contractions and toe-pinch reflexes. Because this dose was chosen as to minimize paralysis (which is not required for analgesia), if movement was observed in the experiment intermittent pushes of pancuronium were provided to ensure motion-free imaging. We refer to this preparation as being in the condition of 'wakefulness' (see 'EEG for assessing brain state') as opposed to 'awake' given that the mice are incapable of gross movements and cannot actively sample odours because of the ventilator (see 'Artificial sniffing').

### Artificial sniffing

To control for potential differences in odour coding due to changes in odour sampling, the mouse's sniffing rhythm was replaced with an 8-Hz fixed inspiration/expiration cycle synchronized in time to odour presentation; this cycle rate mimics known sniffing rates during active odour sampling[44,45]. We adopted a previously developed method in which a cannula was placed into the nasopharynx via the trachea and subsequently attached to a solenoid valve which draws air bidirectionally across the nasal epithelium[46]. The tube was secured to the trachea with a pair of nylon sutures and doused with silicone elastomer for further stability[47]. The distal portion of the tube was then coupled to a computer driven solenoid valve and a vacuum line, providing 50-ms pulses of suction every 75 ms at a flow rate of 100 ml $min^{-1}$.

### EEG for assessing brain state

Anaesthesia is thought to induce a brain-state similar to slow wave sleep that is characterized by large-amplitude fluctuations in the 0.5–4.0 Hz range and the absence of high-frequency activity from 40–100 Hz, which is typically present during wakefulness or behavioural engagement. Because power in the slow and fast frequency bands of the EEG is anti-correlated across these brain states, their ratio has been traditionally used to assign an absolute value to the arousal state of the mouse[48,49]. To compare changes in brain state between wakefulness and anaesthesia and associated changes in odour representation, after completion of awake imaging, some mice were subsequently anaesthetized with a ketamine dose of 50 mg $kg^{-1}$ and 0.5 mg $kg^{-1}$ of medetomidine delivered together intraperitoneally, and the imaging session was immediately repeated. For all experiments, EEG activity was recorded using a silver wire inserted into the dorsal anterior PCx via a 0.5-mm craniotomy. A grounding wire was placed into the contralateral cerebellum. This signal was amplified using an AM Systems 1800 amplifier and digitized with a National Instruments PXie-6341 acquisition card. Signals were detrended and bandpassed (0.5–500 Hz) before computing the EEG power ratio.

### Odour space design

A major goal of this study was to rationally design odour sets such that chemical similarities and differences between odorants in each odour panel could be explicitly titrated. As described previously, to describe odour space we took advantage of 2,584 molecules commonly used in the flavours and perfume industries from http://www.thegoodscentscompany.com/[27]. A large fraction of these molecules are odorous, in that they are less than 300 Da in size and sufficiently hydrophilic and volatile to readily access the environment of the nasal epithelium. This collection contains structurally diverse molecules that vary in carbon chain length, weight, polarizability, hydrophobicity, cyclicity, branching, constituent functional groups, and other chemical attributes. To characterize the physiochemical features of the odours within this large odour collection, we took advantage of a database of 3,705 statistical metrics designed to quantify different molecular physiochemical properties (Dragon, KODE Inc.), including those related to molecular weight, volume, ionization potential, and so on. Using this descriptor database, each of the 2,584 collected molecules were represented by a vector containing 3,705 values (in which each value is a quantitative description of a specific physiochemical feature), thereby constituting an odour chemical space where odour similarity can be expressed as the Euclidean, cosine or correlation distance between any two molecules[5,50]. Of these features, 2,522 are quantified in the Dragon database as continuous variables (for example, molecular weight) and 985 were binarized or categorical (for example, the presence or absence of a N atom). The collection of these inter-odour distances (which holistically capture the quantified physiochemical differences between each odour pair) can be converted into correlation distance matrices (see 'Chemical and activity distance').

### Odour selection

Three ('global', 'clustered' and 'tiled') distinct odour sets were identified, each consisting of 22 odorants. The global odour set contained structurally diverse molecules that span the entire odour space. The clustered odour set consisted of 6 groups of 3–4 molecules, such that all the odours within each group share a chemical functional group (as well as other common chemical features); these groups were designed such that the odours that belong to each group were maximally separated from the odours belonging to all other groups. The tiled odour set included closely related aliphatic molecules that systematically varied along two dimensions; the first was the number of carbon atoms in the chain, and the second was the particular functional group attached to the carbon chain (that is, aldehydes, esters, ketones and acids, all of which are related to each other). Odour selection for the first two odour sets was performed with stochastic optimization (see 'Simulated annealing') to prevent human-induced biases in odour set design. The cost function for the global odour set was designed to maximize separation between all 22 odours (by maximizing the minimum pairwise distance among selected odours). For the clustered odour set, within-group similarity and between-group dissimilarity was maximized by using the silhouette coefficient as the cost function.

### Odour delivery

A 23-valve olfactometer that can deliver up to 22 odorants was used to present odours (Island Motion). The 23rd valve was used to deliver a blank stimulus (no odour) between odour presentations. Custom Arduino software was used to control valve opening and closing, thereby enabling switching between odour vials and the blank vial. This software also controlled the output of two mass flow controllers (MFC). The first MFC delivered a constant carrier flow at 0.8 l $min^{-1}$ of purified air into a common channel; the second MFC supplied a constant flow at 0.2 l $min^{-1}$ of clean air that was injected into an odour vial (see below) and then merged with the carrier flow 1 inch (2.54 cm) in front of the mouse's nose. A larger exhaust fan drew air from the imaging cage that enclosed the rig to prevent cross-contamination.

Monomolecular odours were diluted in di-propylene glycol (DPG) according to individual vapour pressures obtained from www.thegoodscentscompany.com, to give a nominal concentration of 500 ppm. This vapour-phase concentration was further diluted 1:5 by the carrier airflow to yield 100 ppm at the exit port. Odour presentations lasted for two seconds and were interleaved by 30 s of blank (DPG) delivery. The order of presentation of odours was pseudo-randomized for each experiment, such that on any given trial, odours were presented once in no predictable order. Each odour was presented 7–10 times in each experiment.

### Two-photon calcium imaging

High-speed volumetric imaging was performed using a 16-kHz resonant galvo-regular galvo pair (Cambridge Technologies) housed in a custom-designed microscopy rig equipped with 2-inch optics. Acquisition was performed with a large working distance Nikon 16× objective (N16XLWD-PF, 0.8 NA, 3 mm WD) mounted on a high-speed piezo actuator (nPoint 400). A Chameleon laser (Coherent) tuned to 930 nm delivered 50–120 mW of excitation power at the front end of the objective. Emitted fluorescence was detected using Hamamatsu H10770PA-40 PMTs. Scanimage 5 was used for hardware control and data acquisition.

For imaging neuronal cell bodies, acquisition volumes spanned 210 μm in the *Z* axis across PCx L2 and L3. Volumes were split into 6 optical slices each spanning 35 μm of cortex. Volumes were positioned such that two slices resided in L2 and four slices resided in L3. This allowed us to monitor similarly sized populations of neurons in L2 and L3 given the approximately threefold lower cell density of L3 in posterior PCx[51]. We typically discarded a single optical slice that spanned the

boundary between layers to avoid any cross-contamination between layers. For axonal imaging, a single plane was acquired in PCx L1a at 60 Hz and subsequently downsampled by averaging to match the neural acquisition rate.

Note that our imaging fields are in the most anterior portion of posterior PCx. The degree of associational connectivity is known to systematically vary across the anterior-posterior axis of the PCx, with the least associational and most feed-forward connectivity anteriorly[52,53]. We chose to image in the 'middle' of the PCx both because of anatomical constraints in our imaging field in the two-photon configuration, and to ensure the representations we probed would include both feed-forward and associational connectivity. We would expect that if we imaged more anteriorly, we would observe representations that were progressively more 'bulb'-like (given the relative predominance of inputs), and conversely that posterior PCx would deviate more strongly from the bulb (given the relative predominance of associational connectivity); because of surgical constraints, addressing this possibility will require the future development of alternative means of accessing anterior and posterior PCx both pre- and post-synaptically.

### Data inclusion criteria

For experiments involving the global, clustered and tiled odour sets in odour-naive mice, data were analysed from three mice per odour set. For the passive odour exposure experiment, data were analysed from three mice. For bouton imaging, data was analysed from six mice. All mice that satisfied the following pre-determined criteria were included in the study: imaging volumes spanning both piriform cortical L2 and L3 (L1a for boutons) could be imaged continuously for the duration of the experiment; in each cortical layer, at least 150 GCaMP6s-labelled neurons could be identified (500 axonal boutons for axonal imaging); odour-evoked activity persisted over the course of the entire imaging session; and field-of-view drift and motion artefacts could be fully corrected with post hoc image registration. Given the nature of this population imaging study, study sample size was not pre-determined, the experiments were not randomized, and the investigators were not blinded to study conditions.

### Signal extraction

Detection of regions of interest (ROIs), segmentation, and extraction of fluorescence signal was performed using the Suite2p software[54]. This package implements image registration, neuropil fluorescence correction and fluorescence source detection from spatially overlapping ROIs. To accommodate differences in ROI size between axonal boutons and somata, the expected ROI size paramater was set to 5 µm for axonal boutons and 12 µm for somata.

### auROC-based detection of odour responses

Analysis was only performed on neurons that responded, in a statistically significant manner, to at least one odorant. To identify such neurons, we computed the area-under-the-receiver-operator-curve (auROC) statistic for each cell-odour pair. The auROC metric represents the probability that a neuron's response, chosen at random from all presentations of the same odour, will be ranked higher than a randomly chosen sham response obtained using baseline activity. A value of 0.5 indicates no difference between the activity of a neuron during baseline and odour presentation. A value of 1 indicates a perfectly distinguishable excitatory response, whereas a value of 0 indicates a perfectly distinguishable suppressed response. For a single neuron and all presentations of a single odorant, the classifier was provided with the mean fluorescence obtained from 2-s time windows immediately flanking odour onset. A null distribution of auROC values for each cell–odour pair was constructed by randomly permuting the identity of the odour and baseline periods on each presentation. This procedure was repeated 1,000 times. The actual auROC value was deemed significant if it resided outside the 1–99th percentile of the null distribution. Neurons that did not display a significant response to any odours, according to auROC analysis, were excluded from all subsequent analysis. Of those neurons imaged, the fraction of retained neurons (and the absolute number of neurons in each data set) were: global L2 = 854 neurons, 82%; global L3 = 616 neurons, 89%; clustered L2 = 867 neurons, 87%; clustered L3 = 488 neurons, 85%; tiled L2 = 427 neurons, 59%; tiled L2 = 334 neurons, 52%; TeLC tiled L2 = 435 neurons, 51%; TeLC tiled L3 = 590 neurons, 68%; boutons tiled = 3,160 boutons, 68%. Note that the number of neurons deemed responsive by auROC analysis is proportional to the extent to which each odour set captured chemical diversity, with the greatest number of responsive neurons observed in the global odour set, and the fewest observed in the tiled odour set. This distribution of responsive neurons (between 51% and 89%, depending on the chemical diversity in each odour set) is consistent with previous work characterizing response densities and tuning breadths in PCx.

### Gaussian mixture model for response type clustering

Clustering of cell–odour response types was performed for visualization purposes only. Trial-averaged response time courses spanning the odour presentation period were dimensionally reduced by principal component analysis (PCA) to capture 90% of the variance in the data and served as the input to a Gaussian-mixture model, with the optimal number of clusters was assessed using the Bayesian information criterion.

### Lifetime and population sparseness

Lifetime sparseness is a metric reflecting the tuning breadths of individual neurons, with neurons specifically tuned to small numbers of stimuli exhibiting a lifetime sparseness of close to 1; population sparseness is a metric reflecting the density of responses among a population of neurons to a set of stimuli, with less dense responses (that is, fewer neurons or boutons responding to a stimulus set) exhibiting a population sparseness of close to 1. To determine the odour-selectivity of a neuron, the lifetime sparseness metric was computed as previously described[55]:

$$\text{lifetime sparseness} = \frac{1 - \left(\sum_j^N \frac{r_j}{N}\right)^2 \Big/ \left(\sum_j^N \frac{r_j^2}{N}\right)}{1 - \frac{1}{N}}$$

where $r_j$ is the positive odour-evoked change in fluorescence to an odour $j$ relative to baseline and averaged over multiple odour presentations, and $N$ is the number of odours (22 in all odour sets). Inhibitory responses were zeroed (for this analysis only). Lifetime sparseness reflects the kurtosis of the tuning profile of a neuron and ranges from 0 to 1. Highly peaked, narrow tuning profiles yield values close to 1 and represent neurons that respond strongly and selectively to few odours. Values close to 0 indicate equal responsiveness to a large fraction of the odour set. Population sparseness for each odour was calculated using the same formula used for lifetime sparseness, but in this case, $j$ indexes a neuron instead of an odour.

### Signal and ensemble correlations

The extent to which any two neurons have similar odour preferences can be assessed by computing the Pearson's product moment correlation between their trial-averaged odour response profiles (tuning curves). This is typically referred to as a 'signal' correlation. The tuning curve of each neuron was represented as a vector containing $N$ elements, where $N$ is the number of odours in the stimulus set. Each entry in this vector corresponds to the odour-evoked change in fluorescence relative to baseline and averaged over all presentations. For each neuron, responses across odours were $z$-scored. Populations were defined as all neurons that responded to at least one odour according to the auROC analysis.

We also wished to compute the similarity in odour responses exhibited by different odour-evoked ensembles of PCx neurons or boutons. We refer to this here as 'ensemble' correlation. In these analyses, we computed the Pearson's correlation between the population responses

to every pair of odours in our panel. The population response of each odour was represented as a vector containing $N$ elements, where $N$ is the number of neurons/boutons in the population. Each entry in this vector represents the trial-averaged response of each single neuron/bouton to the corresponding odour. For each neuron/bouton, responses across odours were $z$-scored. Populations were defined as all neurons/boutons that responded to at least one odour according to the auROC analysis.

### Chemical and activity distance

Pairwise odour distances (1 − Pearson's $r$) in neural activity space were computed between odour vector pairs where each matched vector entry corresponded to a single neuron's trial-averaged response to the corresponding odour. This procedure was applied to neural populations from individual mice or to pseudo-populations of neurons built by pooling all responsive neurons from all mice for each layer and odour set. In chemical space, correlation distances between odour pairs were computed identically, except each vector entry (matched across odours) represented the odour-specific value assigned by a physiochemical descriptor. For presentation purposes, distance matrices were sorted using hierarchical clustering. For the global odour set, all odours were sorted collectively. For the clustered odour set, odours were sorted within each functional class first followed by sorting on functional classes. For the tiled odour set, functional group classes were sorted, but odours within each class were ordered according to increasing chain length. Row and column ordering of all activity and chemistry distance matrices is preserved across figures. Note that for all correlation analyses, both inhibitory and excitatory responses were included.

### UMAP embedding

For visualizing odour relationships in neural data, population responses were embedded in two dimensions using UMAP[56]. Selection of optimal embedding settings was accomplished by minimizing the mean-squared error between correlation distance matrices built from data projected on the UMAP dimensions and those corresponding to the input data. Simulated cortical responses from the feed-forward models were processed in a similar manner. Because UMAP imposes an arbitrary rotation on projected data, each embedding was aligned to a reference using the orthogonal Procrustes transformation. For embeddings of pseudopopulation data for the tiled odour set across boutons as well as neural and simulated cortical data, bouton data served as the reference. For aligning embeddings obtained from individual mice, the orthogonal Procrustes transform (rotation and reflection only) was performed iteratively across mice in a pairwise manner[57]. Note that these embeddings are meant to visualize odour relationships (and are complemented by quantitative metrics); pairwise relationships cannot be changed by any of the rotations used herein to align embeddings to each other.

### Distance-based nearest neighbour decoding and classification

To test whether PCx odour relationships are invariant across individuals, we asked whether we could identify any given odour from one mouse based upon the pairwise odour relationships observed in other mice. To decode odour identity based on odour relationships, nearest neighbour classifiers were trained on odour distances from two mice and tested on odour distances obtained from a held-out mouse, such that each mouse was tested once. For each such classifier, 100 bootstrap iterations were performed. For each iteration, correlation distance matrices were constructed using a randomly sampled neural ensemble containing 50 neurons. In each condition, each distance matrix represented all pairwise correlations between trial-averaged population responses (see 'Chemical and activity distance'), such that any given training or testing odour was represented as a vector containing 21 pairwise distances. For a single run of the classifier, reported accuracy represents the fraction of odours that were correctly identified.

### Distance covariance analysis

Distance covariance analysis (DCA) belongs to a set of statistical methods that seek to identify shared dimensions of variability between two different data sets. DCA—an extension of canonical correlation analysis—was developed for identifying related dimensions of activity across two or more populations of neurons[58]. To measure the similarity of cortical odour relationships between individual mice, DCA was performed on response data (neurons by odour-trial) from all individual mice exposed to the same set of odours (code supplied with the reference). The output consisted of a set of orthogonal dimensions (one set per mouse) and associated DCA statistics ranked from highest to lowest contribution to common activity between individuals. Each dimension was evaluated for significance by permutation testing. The null distribution of DCA statistics was constructed by shuffling the sequence of odour responses across all neurons in each mouse to destroy between but not within-mouse relationships. A dimension was deemed significant if its associated statistic was higher than the 95$^{th}$ percentile of the null distribution built from 100 permutations. Three to six dimensions were typically retained. Because DCA is not deterministic, this procedure was subjected to 100 independent restarts. The reported results correspond to the best modelling run. The fraction of an individual's neural variance that could be explained by the shared embedding was determined by calculating the total accounted variance after regressing each neuron's activity on the set of DCA dimensions.

### Silhouette coefficient

The degree of clustering in odour correlation distance matrices was evaluated using $k$-means clustering and the silhouette coefficient. Correlation distances were computed between trial-averaged population responses to all 22 odours in the tiled odour set. Correlation distance matrices containing all pairwise odour distances were projected onto 21 principal components and subjected to $k$-means clustering. For this set of labelled data, the silhouette coefficient assigns a single value ranging from −1 (overlapping diffuse clusters) to 1 (compact, well-separated clusters) that represents the average silhouette score computed on an odour-by-odour basis: for an odour $i$, its score, $S_i$, is defined as $(b_i - w_i)/\max(w_i, b_i)$, where $w_i$ is the average Euclidean distance between odour $i$ and all other odours with the same class label, and $b_i$ is the average distance between odour $i$ and all odours in the next nearest class. Qualitatively similar results between experimental conditions were obtained by running $k$-means and cluster evaluation directly on full population response data or by obtaining $k$-means labels from full population data and computing the silhouette coefficient using these labels on PCA embeddings of correlation distance matrices.

### Effective dimensionality

Effective dimensionality (ED) of a population of neurons, a quantity reflecting the number of principal components required to capture the odour-evoked neural variance, was defined as previously described[59,60]. In brief, for each experimental condition and for model cortical activity, ED was quantified from trial-averaged population responses (neural data only) after mean-centring units across odours. ED reflecting variance in similar ensemble sizes were calculated as averages across randomly chosen, 300-unit ensembles (100 bootstraps).

### Hierarchical clustering

Dendrograms depicting the reconfiguration of odour relationships across boutons, PCx, TeLC, and the feed-forward random connectivity model PCx were constructed directly from correlation distance matrices associated with each experiment. First, each correlation matrix was projected, using PCA, onto $K$ dimensions, where $K$ is the number of dimensions required to explain 95% of the variance in correlation distances. The resulting embedding expresses the contributions of each odour to the prominent similarity or dissimilarity modes in the

original correlation distance matrix. Dendrograms were built by hierarchically clustering this data using Euclidean distance and Ward's linkage. Clustering similarity between dendrogram pairs was assessed using the Cophenetic correlation coefficient after topologically aligning each pair.

### Feed-forward connectivity model

To assess whether the observed cortical odour responses are expected under a random feed-forward model we simulated the OB–PCx network using a previously established model[19]. In our implementation of this model (which hews as closely as possible to the published model), the OB and PCx layer contained 1,000 and 100,000 units, respectively, feed-forward connections were assigned randomly and can be either excitatory or inhibitory, and each cortical neuron was 'innervated' by a random 20% of excitatory OB units and a random 40% of inhibitory units. Excitatory and inhibitory connection weights were set to 1 and −0.5 respectively, providing each PCx unit with balanced excitatory/inhibitory innervation. Odour-evoked activity in the OB layer was simulated from a log-normal multivariate distribution defined by population-mean response amplitudes and covariance obtained from bouton activity. Model PCx neurons linearly summed their inputs and are zero-rectified. The odour-average response fraction of model PCx units was adjusted to 8% to match the fraction of excitatory responses observed in PCx (detected by auROC analysis) on average across all odours and subjects in our experimental data.

### Decoding analysis

Linear SVM classifiers were trained to predict either odour identity or odour class (based on chain-length) in the tiled odour set on the basis of odour-evoked population activity.

For discrimination of odour identity (Fig. 4a), all neurons or boutons that responded to at least one odour in the tiled odour set (according to auROC analysis) were pooled to build three pseudo-populations of neurons or boutons (boutons, L2, L3). *Z*-scored responses of a population of up to $n$ randomly selected neurons or boutons (the maximum common number of neurons recorded across the layers) were then considered, given $t$ presentations of $j$ odours as a matrix X with $n$ rows (neurons/boutons) and $t \times j$ columns (trials/instances × odours/classes). Each column of this matrix was thus a vector of $n$ responses, one for each neuron/bouton in response to a given odour in each trial. Each decoding session started with a split of the matrix X into a training and test set: the training set included $0.9 \times t$ randomly chosen trials for each class and the test set comprised the $0.1 \times t$ held out trials for each class (that is, a standard 9:1 training:testing split). This procedure, which is instantiated as part of the standard LIBSVM library (http://www.csie.ntu.edu.tw/~cjlin/libsvm/), allows us to use a binary classification algorithm (such as an SVM) to compare multiple classes. In any given experiment, the train-test procedure was iterated 100 times (with training and test data randomly chosen on each iteration) to cross-validate classifier performance. For differently sized subpopulations of neurons or boutons, a randomly selected subset of neurons or boutons was used for each cross-validation cycle, and at the end of this procedure the outcomes of each individual iteration were averaged to generate a measure of classification accuracy across all restarts; this is the overall measure that is reported in the main text (Fig. 4a). The hyperplanes for each classifier were determined using the LIBSVM library with a linear kernel, the C-SVC algorithm, and cost $c$. Cost $c$ is the only free parameter for a linear kernel, and it was found by a grid search on an initial data set including 50 randomly chosen neurons/boutons from each dataset in order to maximize the accuracy of the decoder classification.

For Fig. 4b, classifiers were trained on 21 out of 22 odours in the tiled odour set, with all trials associated with any training odour assigned to 1 out of 21 classes. SVM class predictions for each held-out odour were converted to confusion probabilities (the probability that any given held-out odour is associated with any other of 21 odours) using the Python scikit-learn library[61] implementation of Platt scaling[62]. Class probabilities for each tested odour were rank-ordered before averaging across all odours.

For Fig. 4c, classifiers were trained to predict the class (either short-chain or long-chain) of a held-out odour after training on a single short-chain–long-chain odour pair. All odour trials were presented on each train-test iteration and accuracy was determined as the fraction of correctly labelled held-out trials. For each randomly chosen subpopulation of neurons, on each of 100 restarts, training and testing was performed on all possible short-chain–long-chain odour pairs and associated held-out odours. Cross-validated generalization accuracy corresponds to the average performance across all restarts and folds of the data. The short-chain class contained aldehydes: propanal, butanal and pentanal; ketones: propanone, butanone and pentanone; esters: ethyl and butyl acetate. The long-chain class contained aldehydes: heptanal and octanal; ketones: hexanone, heptanone and octanone; esters: pentyl and hexyl acetates. The acid block is excluded for this analysis.

### Lasso optimization

For finding small, optimal combinations of Dragon descriptors that predict neural odour relationships, an L1-regularized optimization routine was designed to maximize the correlation between matched odour-pair distances across chemical and neural spaces. During each step of optimization ('L-BFGS-B' gradient descent), descriptor weights (0 bounded) were modified and chemical distances were recomputed. The optimization objective sought to minimize the residual sum of squares between the modified descriptor distances and corresponding neural odour distances. The Lasso component set the sparseness of the final solution and was selected for each model by cross-validation. Models were trained and validated on individual odour sets containing 22 molecules with fivefold cross-validation (random splits) such that on any split of the data, $17 \times (17-1)/2$ odour pairs made up the training set and $5 \times (22-5)$ odour pairs comprised the validation set. For assessing generalization to other odour sets, models were retrained with all 22 odours before testing. Because the global and clustered odour sets share odours, overlapping odours were removed from training when cross-applying to the held-out odour set. For within-odour set cross-validation and cross-application to the tiled odour set all odours were included. For Extended Data Fig. 5c, we sought to determine the relative contribution of the full set of descriptors belonging to the 'molecular properties' block of the Dragon database to bouton/cortical relationships; for this analysis, optimization was performed without imposing L1-regularization.

### Simulated annealing

Stimulated annealing was used for odour set design, as well as for predictive modelling of neural odour relationships. Simulated annealing is a well-validated Monte Carlo sampling variant designed for stochastic optimization[63]. Simulated annealing optimization works by slowly decreasing a pre-specified cost function over the course of sampling, thereby enabling good initial coverage of solution space and progressive convergence on a global optimum. All simulated annealing routines were implemented using the open-source Python package simanneal available at https://pypi.python.org/pypi/simanneal. For odour set selection, the number of features was reduced, via PCA, such that the transformed odour space accounted for 95% of the original variance. Optimization for the global and clustered odour sets (see 'Odour selection') was carried out using Euclidean distance in this reduced space.

In addition, our findings using Lasso optimization were verified using simulated annealing; here, the simulated annealing objective was designed to identify small sets of Dragon physiochemical features describing a set of molecules such that molecular distances in chemical space were maximally correlated with corresponding odour distances in neural space. Qualitatively similar findings using simulated annealing were observed as reported in the manuscript using Lasso optimization

(data not shown). By design, the chemical variation in the tiled odour set, queried here, is focused on chain length and functional group; while the observation that bulb and cortex differentially encode information about these chemical features clearly demonstrates a representational transformation, it does not imply that chain length or functional group per se are privileged in either of these brain regions relative to the multitude of chemical features not captured by the tiled odour set.

### Cross-habituation for assessing perceptual odour similarity

C57 males (5–6 weeks old) obtained from Jackson laboratories were housed on a reverse light schedule for 48 h before beginning behavioural experiments. Established procedures for assessing odour similarity were slightly modified[64]. Twenty-six pairwise comparisons were obtained, with twelve odorants serving as the first odorants in each comparison: butanal versus pentanal or propyl acetate; butanoic acid versus heptanoic acid or butanone; butanone versus butanoic acid or propyl acetate or butanal; heptanal versus octanal, or pentyl acetate; heptanone versus pentyl acetate or heptanal or hexyl acetate or octanal; hexyl acetate versus pentyl acetate or octanone or octanal or octanoic acid; octanal versus butanal or heptanal or octanone; octanoic acid versus octanal; octanone versus octanoic acid; pentyl acetate versus hexyl acetate; propanoic acid versus butanoic acid; propyl acetate versus butanone or butanal or butanoic acid.

Short-chain pairwise odour comparisons, different functional groups (asterisks indicate the same pair was presented at different positions in the triplet): butanone versus butanal; butanone versus butanoic acid*; propyl acetate versus butanone*; propyl acetate versus butanal*; propyl acetate versus butanoic acid.

Long-chain pairwise odour comparisons, different functional groups (asterisks indicate the same pair was presented at different positions in the triplet): heptanal versus pentyl acetate; octanal versus octanone; heptanone versus pentyl acetate; heptanone versus heptanal; heptanone versus hexyl acetate; heptanone versus octanal; octanone versus octanoic acid; pentyl acetate versus hexyl acetate*; hexyl acetate veresus octanone; hexyl acetate versus octanal; hexyl acetate versus octanoic acid; octanoic acid versus octanal.

Remaining pairs: heptanal versus octanal; octanal versus butanal; butanal versus pentanal; propionic acid versus butanoic acid; butanoic acid veresus heptanoic acid.

Because three odours were presented to each mouse, two adjacent odour pairs were included in analysis from each mouse. Presentation order effects were considered by swapping the order of any given triplet in different experiments. As indicated above, for some comparisons the same pair was presented at different positions in the triplet. Investigation time was scored manually, using video footage obtained during each experiment. Scoring was done blinded to experimental conditions, and with no knowledge of odour identity. Odour investigation was defined as periods of orienting to the odour source on the half of the cage containing the odour source as well as by stereotyped bouts of sniffing and associated head-bobbing.

Perceptual similarity (behavioural distance) between two odours was defined as the difference in time spent investigating the first odour in a pair during its last presentation and the investigation time associated with the first presentation of the subsequent odour (Extended Data Fig. 8). In Fig. 4d, linear regression was used to relate behavioural to neural distance. Because behavioural distance increases monotonically but not necessarily linearly with neural distance, we also used Spearman $\rho$, which measures correlation based on ranks and is less restrictive than linear regression. Three to twelve mice were used for each pairwise comparison (eight mice on average per triplet experiment). Each mouse was used for a single set of odour comparisons.

### Passive odour exposure

C57 males (5–6 weeks old) were housed on a reverse light schedule for 48 h before behavioural training. Group-housed mice were subjected to daily odour exposures for a period of two weeks. On each training session (30 min; 3 times per day, 14 consecutive days) mice were simultaneously presented with two short-chain aldehydes (propanal, butanal) and two short-chain ketones (propanone, butanone) for 1 min separated by a 5-min inter-stimulus-interval. Odour delivery was designed to closely approximate odour presentation during cortical imaging. In brief, odours were delivered to the home cage using a custom-built olfactometer consisting of an activated-carbon purification unit, master air flow controllers, and a valve bank coupled to four odour vials and one blank vial. Flow rates for carrier and odour lines were set to 0.8 and 0.2 l $min^{-1}$ respectively. Monomolecular odorants were diluted in DPG according to individual vapour pressures to yield a final concentration of 100 ppm at the output of the olfactometer. During odour delivery, odorants were mixed in air phase by simultaneous opening of all four valves. During the inter-stimulus-interval, air was passed through the blank odour vial containing only DPG. Mice were not subject to this protocol on the day of imaging.

### Measuring changes in cortical odour representations after mixture exposure

Cortical representations of all 22 odours of the tiled odour set were obtained after cessation of behavioural training. Single neuron and population representations of the target aldehydes (propanal and butanal) and target ketones (propanone and butanone) were compared to data obtained from odour-naive mice exposed to the tiled odour set. Off-target control comparisons were made between chain-length matched esters and acids (ethyl acetate and propyl acetate versus propanoic acid and butanoic acid) as well as between target ketones and off-target long-chain aldehydes (heptanal, octanal).

For comparing changes in response profiles of individual neurons across the target classes, a class preference index was assigned to each neuron using ROC binary classification. The trial-averaged responses of each neuron were labelled as either aldehydes or ketones, resulting in a single auROC value reflecting the degree of discriminability between classes. The class preference index was obtained by rescaling auROC values from a range of 0 to 1 to a range of −1 to 1 with 0 representing low discriminability. Because the class preference index combines both the magnitude and frequency of responses, a neuron with weak preference for a single class could be strongly and uniformly responsive or non-responsive to the target odours. We therefore limited analysis to neurons exhibiting at least one response to any short-chain aldehyde or ketone of magnitude greater than 2 s.d. above the mean response across all 22 presented odours. Changes to odour similarity at the population level were assessed by comparing the correlation distance between odour pairs across classes. Because differences in the average magnitude of ensemble correlations (which are not relevant to the pairwise restructuring we focus on herein) may uniformly bias comparisons between experimental conditions, before computing pairwise correlation distances (see 'Chemical and activity distance'), the trial-averaged tuning profile of each neuron was initially centred on its mean).

### Descriptor relevance

The chemical descriptors in Supplementary Table 1 identified by Lasso optimization afford an algorithmic representation of chemical structure. However, each descriptor incorporates some information about semantic molecular properties, such as molecular weight, electronegativity, polarizability, ionization potential, molecular volume and hydrophobicity. The relevance of each descriptor, obtained from the (Dragon, KODE Inc.) website https://chm.kode-solutions.net/products_dragon_descriptors.php, is presented next to the descriptor name.

### Statistical tests

For comparing two normal independent distributions, the Student's *t*-test (two-sided) was used. For comparing two independent distributions when normality cannot be assumed, significance was assessed by permutation testing or using the two-sided Wilcoxon rank sum test. The Kolmogorov–Smirnov test was used to determine equivalence

between two distributions. For testing significance of a single statistic against null distributions obtained by permutation, the true value was deemed significant if it resided outside the 5th–95th percentile of the null statistic distribution. Error bars refer to 95th confidence interval, s.e.m. or s.d. as indicated in the figure legends. For regression modelling, confidence intervals are computed over bootstraps (with replacement) of the data. For establishing correspondence between two distance matrices, Pearson's product moment correlation was used on the upper diagonal of each set of measurements.

### Reporting summary

Further information on research design is available in the Nature Research Reporting Summary linked to this paper.

## Data availability

All data will be posted to Github or made available upon reasonable request (www.github.com/dattalab).

## Code availability

All code will be posted to Github or made available upon reasonable request (www.github.com/dattalab).


38. Challis, R. C. et al. Systemic AAV vectors for widespread and targeted gene delivery in rodents. *Nat. Protoc.* **14**, 379–414 (2019).
39. Bruno, R. M. & Sakmann, B. Cortex is driven by weak but synchronously active thalamocortical synapses. *Science* **312**, 1622–1627 (2006).
40. Minamisawa, G., Funayama, K., Matsuki, N. & Ikegaya, Y. Intact internal dynamics of the neocortex in acutely paralyzed mice. *J. Physiol. Sci.* **61**, 343–348 (2011).
41. Simons, D. J. & Carvell, G. E. Thalamocortical response transformation in the rat vibrissa/barrel system. *J. Neurophysiol.* **61**, 311–330 (1989).
42. Maklad, A., Quinn, T. & Fritzsch, B. Intracranial distribution of the sympathetic system in mice: DiI tracing and immunocytochemical labeling. *Anat. Rec.* **263**, 99–111 (2001).
43. Doevendans, P. A. J., Daemen, M. J., de Muinck, E. D. & Smits, J. F. Cardiovascular phenotyping in mice. *Cardiovasc. Res.* **39**, 34–49 (1998).
44. Carey, R. M. & Wachowiak, M. Effect of sniffing on the temporal structure of mitral/tufted cell output from the olfactory bulb. *J. Neurosci.* **31**, 10615–10626 (2011).
45. Kepecs, A. & Uchida, N. The sniff as a unit of olfactory processing. *Chem. Senses* **31**, 167–179 (2006).
46. Cheung, M. & Carey, R. A method for generating natural and user-defined sniffing patterns in anesthetized or reduced preparations. *Chem. Senses* **34**, 63–76 (2009).
47. Moldestad, O., Karlsen, P., Molden, S. & Storm, J. F. Tracheotomy improves experiment success rate in mice during urethane anesthesia and stereotaxic surgery. *J. Neurosci. Methods* **176**, 57–62 (2009).
48. Ecker, A. S. et al. State dependence of noise correlations in macaque primary visual cortex. *Neuron* **82**, 235–248 (2014).
49. Goard, M. & Dan, Y. Basal forebrain activation enhances cortical coding of natural scenes. *Nat. Neurosci.* **12**, 1444–1449 (2009).
50. Ma, L. et al. Distributed representation of chemical features and tunotopic organization of glomeruli in the mouse olfactory bulb. *Proc. Natl. Acad. Sci. USA* **109**, 5481–5486 (2012).
51. Srinivasan, S. & Stevens, C. A quantitative description of the mouse piriform cortex. Preprint at https://www.bioRxiv.org/content/ 10.1101/099002v1.full (2017).
52. Hagiwara, A., Pal, S. K., Sato, T. F., Wienisch, M. & Murthy, V. N. Optophysiological analysis of associational circuits in the olfactory cortex. *Front. Neural Circuits* **6**, 18 (2012).
53. Luna, V. M. & Morozov, A. Input-specific excitation of olfactory cortex microcircuits. *Front. Neural Circuits* **6**, 69 (2012).
54. Pachitariu, M., Stringer, C., Dipoppa, M. & Schröder, S. Suite2p: beyond 10,000 neurons with standard two-photon microscopy. Preprint at https://www.bioRxiv.org/content/10.1101/061507v2 (2017).
55. Willmore, B. & Tolhurst, D. J. Characterizing the sparseness of neural codes. *Network* **12**, 255–270 (2001).
56. McInnes, L., Healy, J. & Melville, J. UMAP: Uniform Manifold Approximation and Projection for Dimension Reduction. Preprint at https://arXiv.org/abs/1802.03426 (2018).
57. Haxby, J. V. et al. A common, high-dimensional model of the representational space in human ventral temporal cortex. *Neuron* **72**, 404–416 (2011).
58. Cowley, B. et al. Distance Covariance Analysis. *Proc. 20th International Conference on Artificial Intelligence and Statistics* **54**, 242–251 (2017).
59. Litwin-Kumar, A., Harris, K. D., Axel, R., Sompolinsky, H. & Abbott, L. F. Optimal degrees of synaptic connectivity. *Neuron* **93**, 1153–1164 (2017).
60. Abbott, L. F., Rajan, K. & Sompolinsky, H. Interactions between intrinsic and stimulus-evoked activity in recurrent neural networks. Preprint at https://arXiv.org/abs/0912.3832 (2009).
61. Pedregosa, F. et al. Scikit-learn: Machine Learning in Python. *J. Mach. Learn. Res.* **12**, 2825–2830 (2011).
62. Platt, J. Probabilistic outputs for support vector machines and comparisons to regularized likelihood methods. *Adv. Large Margin Classifiers* **10**, 61–74 (1999).
63. Kirkpatrick, S., Gelatt, C. D. Jr & Vecchi, M. P. Optimization by simulated annealing. *Science* **220**, 671–680 (1983).
64. Wilson, D. A. & Linster, C. Neurobiology of a simple memory. *J. Neurophysiol.* **100**, 2–7 (2008).



**Acknowledgements** We thank members of the Datta laboratory, J. Pillow, R. Axel, L. Abbott, A. Litvin-Kumar, C. Schoonover, A. Fink and V. Ruta for comments on the manuscript, S. Knemeyer for technical illustrations, and N. Bhagat for laboratory assistance. We thank N. Mathur for assistance with viral delivery of GCaMP6s. We thank A. Giessel for early development of tools for image acquisition and analysis. We thank O. Mazor and P. Gorelik from the Research Instrumentation Core Facility and Ludo Cacheux for engineering support. Core facility support is provided by NIH P30 grants HD18655 and NS072030. S.R.D. is supported by fellowships from the Vallee Foundation, by grants RO11DC016222 and U19 NS112953 from the National Institutes of Health and by the Simons Collaboration on the Global Brain. S.P. is supported by grant NS108410 from the National Institutes of Health. D.C. is supported by a Bertarelli Foundation Fellowship. S.L.P. is supported by grant DA036922 from the National Institutes of Health and the Stuart H.Q. and Victoria Quan Fellowship. G.I. is supported by the Armenise Foundation Career Development Award.


**Author contributions** S.L.P. and S.R.D. conceived and designed the experiments. S.L.P. performed imaging experiments and K.D. performed behavioural experiments. G.I. assisted with analysis and performed single-unit recordings to validate the TeLC experiment. D.B. generated reagents and performed infections and histology for the bulbar afferent experiments, and helped to modify and test reagents for the TeLC experiment. K.F. provided reagents and guidance for the TeLC experiment. S.L.P., G.I. and D.C. analysed the data. S.P. provided guidance about population analysis. S.L.P., G.I. and S.R.D. wrote the manuscript.

**Competing interests** The authors declare no competing interests.

**Additional information**


**Supplementary information** is available for this paper at https://doi.org/10.1038/s41586-020-2451-1.



**Correspondence and requests for materials** should be addressed to S.R.D.



**Peer review information** *Nature* thanks Vijay Balasubramanian and the other, anonymous, reviewer(s) for their contribution to the peer review of this work.

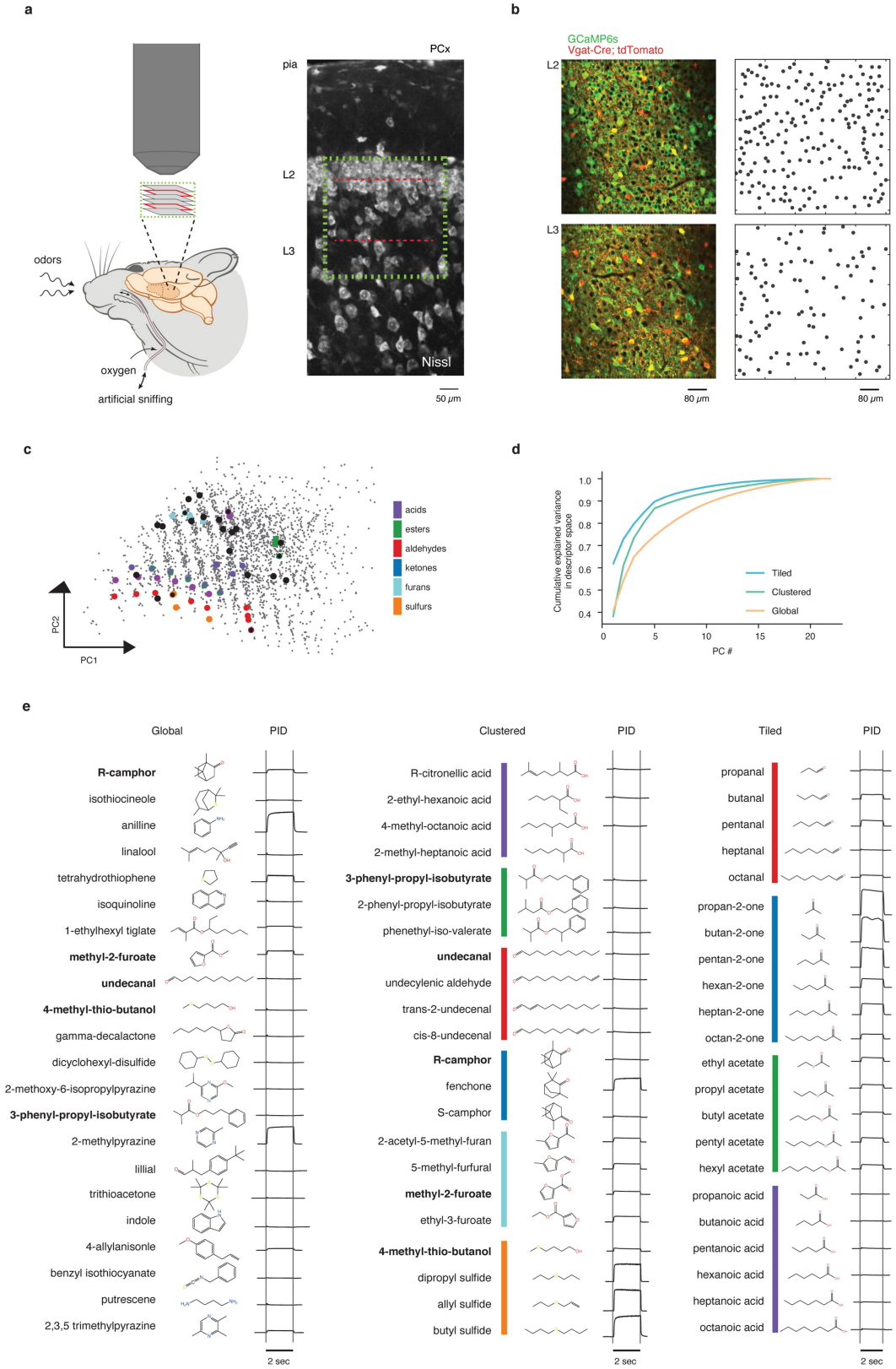


**Extended Data Fig. 1** | See next page for caption.

**Extended Data Fig. 1 | Volumetric population imaging of PCx L2 and L3 during wakefulness using rationally designed odour sets. a**, Left, cartoon of the volumetric multi-photon imaging approach used to characterize odour responses in PCx in wakeful, semi-paralysed mice (Methods). Right, approximate position of an imaging volume (green dotted line) in a typical experiment superimposed on a Nissl-stained coronal section through PCx. Scanning volumes were oriented to acquire similarly sized cortical populations in L2 and L3 (red dotted lines), despite decreased neuron density in L3 (Methods). Imaging was performed in the most anterior portion of the posterior PCx. **b**, Sample fields of view for a single imaging session. PCx L2 is depicted on top; PCx L3 on bottom. Segmentation masks associated with each layer are shown on the right. **c**, Global, clustered and tiled odour sets superimposed on the collection of odours constituting odour space as defined by principal components analysis (Methods). Global odours are indicated by black dots; tiled and clustered odour sets via the indicated colour code. **d**, Plot of the amount of molecular variance contributed by each additional principal component for each odour set in descriptor space; this analysis reveals that each odour set tiles odour space at a distinct level of resolution. **e**, Molecular structures and associated photoionization detector (PID) signals of the odours comprising the global, clustered and tiled odour sets. These PID traces are shown to illustrate the controlled kinetics of the olfactometer only; because detector reports depend on the ability of an odour to be photo-ionized, the relative amplitudes of the traces between odours are not meaningful. For example, heavy aliphatics elicit a minimal PID response because their photo-ionization energies lie outside the range of the detector; however, odours with low or absent PID traces still induced cortical activity in 5–20% of the imaged population, consistent with effective odour delivery. Five odours are shared between the global and clustered odour sets. These are indicated by bold lettering (and in **c**, as black circles with coloured edges). Colour code as in **c**.

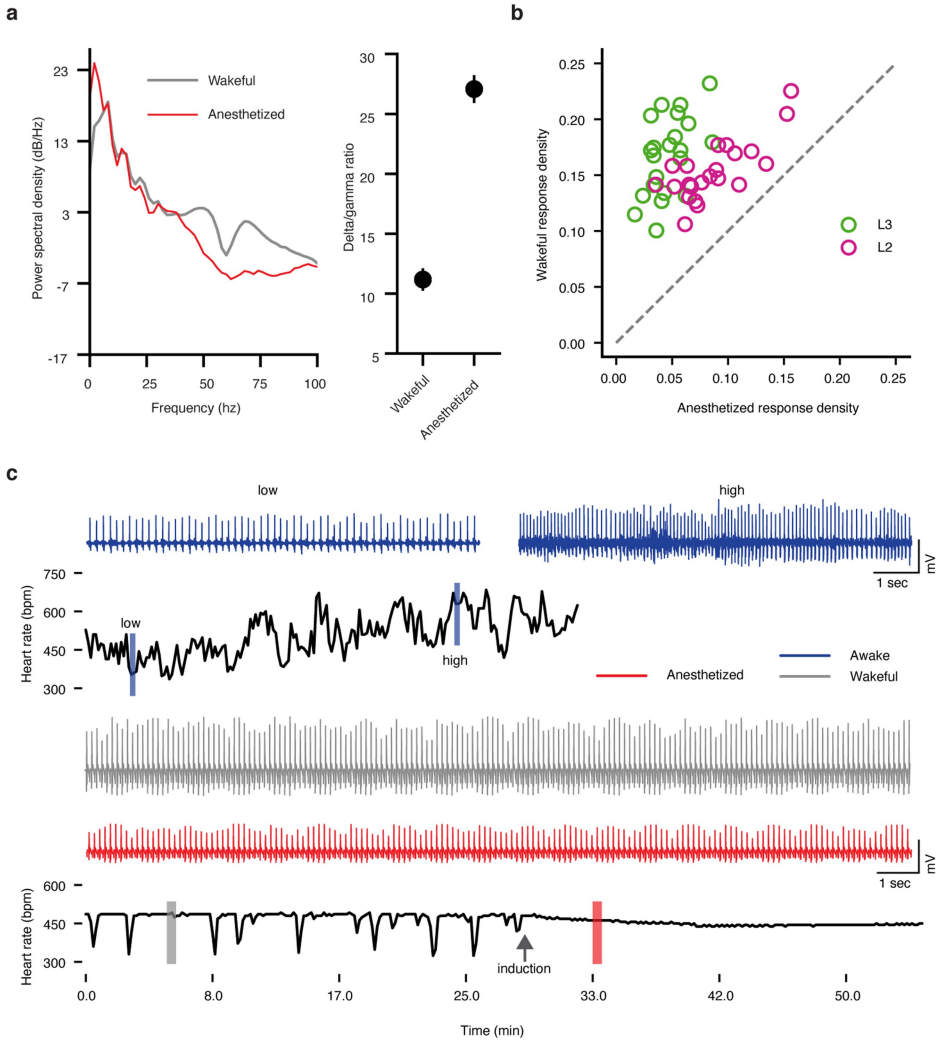


**Extended Data Fig. 2 | Odour responses in PCx are substantially altered by anaesthesia. a**, Left, EEG power spectral density plot from an individual subject depicting differences in cortical state between ketamine–medetomidine anaesthesia and wakefulness (Methods). Under anaesthesia, the EEG signal is enriched in the delta band (0.5–4 Hz) at the expense of high frequency (40–100 Hz) gamma oscillations; by contrast, gamma activity increases and delta activity decreases during wakefulness. Right, summary of differences in EEG power content expressed as delta/gamma ratio during anaesthesia and wakefulness averaged from four subjects. Error bars indicate s.e.m. **b**, Comparison of the fraction of responsive neurons (obtained from the population of neurons that respond to at least one odour during the wakefulness) (Methods) to the tiled odour set in the same field of view (obtained from PCx L2 and PCx L3) during the awake state and under anaesthesia. Responses are defined according to auROC analysis (Methods). Each dot represents a single odour (L2: 504 neurons, L3: 418 neurons). **c**, Top, black trace represents heart rate (average over 10 s, non-overlapping windows) recorded from an awake mouse in the home cage. Blue traces are example raw heart rate (HR) signal indicating the range of heart rate fluctuations observed during the awake state. The high variability in heart rates (which span approximately 350 to 650 beats per min) reflects ongoing behaviour in the awake mouse. Bottom, as in the top panel, but for heart rate recorded during wakefulness and after induction of ketamine–medetomidine anaesthesia (Methods). Grey arrow indicates time of induction. Grey and red rectangles and associated inset traces are 20-s segments of real-time heart-rate signal. During wakefulness, fluctuations in heart rate remain within a physiologically normal range of 300–500 beats per min, without any detectible episodes of tachycardia (Methods). Periodic large-amplitude dips in the recorded heart rate during wakefulness reflect moments when pharmacological agents are being administered, which briefly interrupts the heart rate monitor.

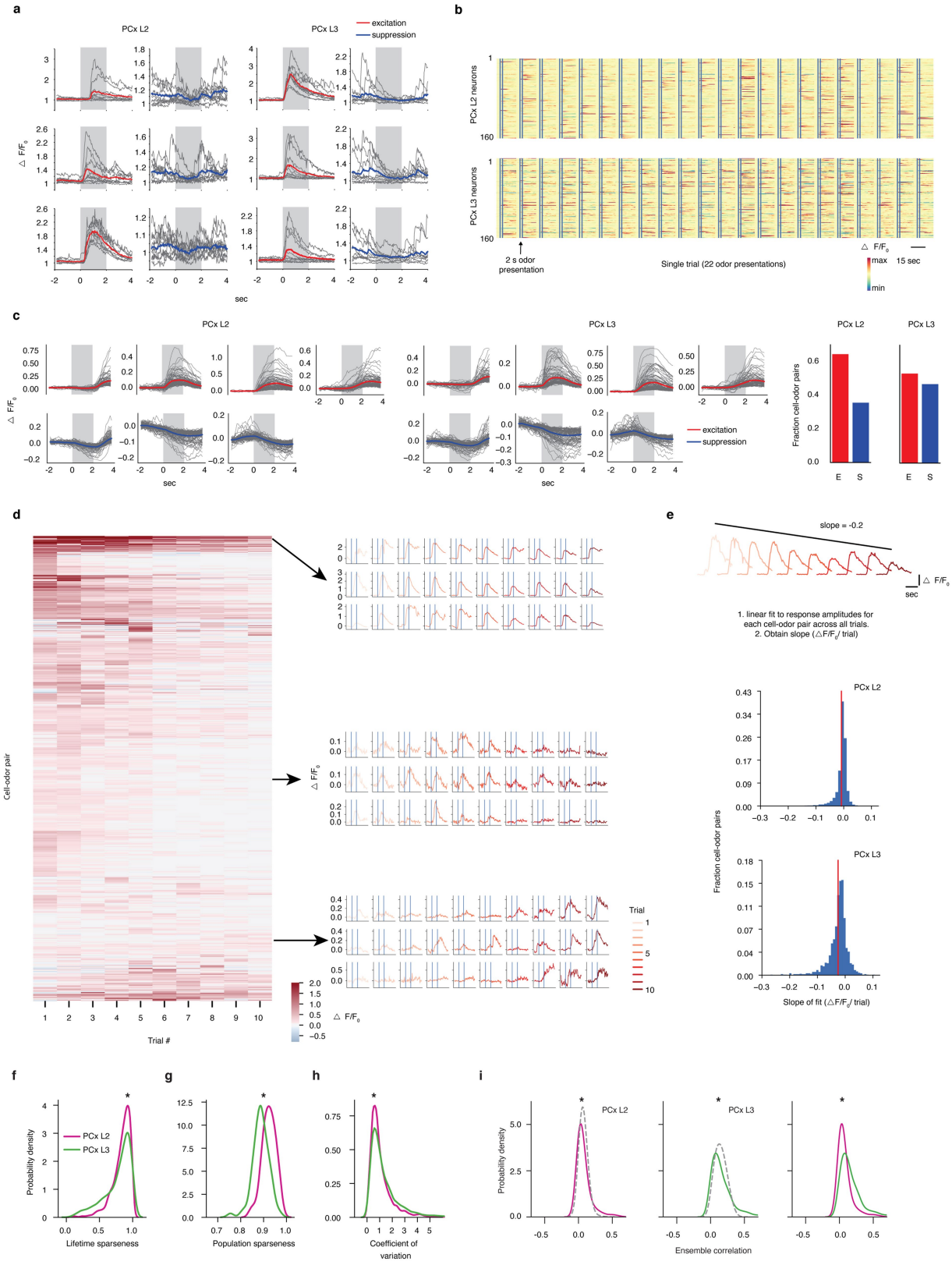


**Extended Data Fig. 3** | See next page for caption.

**Extended Data Fig. 3 | PCx L3 neurons exhibit denser, broader and more reliable odour responses than neurons in PCx L2. a**, Examples of odour-evoked excitation and suppression in PCx. Each panel corresponds to a single cell-odour pair. Grey lines represent individual trials. Coloured overlays represent trial-mean activity. Shaded grey rectangles delimit the odour presentation period. **b**, Trial-averaged population response raster depicting odour-evoked activity in response to 22 odours (global odour set) across L2 and L3. Responses are $\Delta F/F_0$ with redder colours indicating excitatory transients and bluer colours indicating odour-evoked suppression. *x* axis is time; double vertical bars delimit 2-s odour presentation periods. **c**, Response types observed in L2 and L3 (clustered odour set). Individual panels correspond to clusters identified using a Gaussian mixture model (Methods). Grey traces correspond to trial-averaged cell-odour pairs. Coloured overlays represent mean response time course associated with each cluster. Right, fraction of all cell-odour pairs exhibiting excitation or suppression. **d**, Response amplitudes of cell-odour pairs obtained from PCx L3 depicted on a trial-by-trial basis. Each row represents the response of a given neuron to 10 consecutive presentations of the same odour. Neurons are sorted hierarchically using average linkage and correlation distance. Despite the presence of some habituation in response to several presentations of the same odorant across the experiment, habituation does not appear uniform across the neural population nor does it appear to dominate neural responses to odours. Different groups of neurons were identified with maximal responses to an odour peaking at different times across the experiment; see examples depicted on the right. Each row of traces corresponds to a single cell-odour pair. **e**, At the population level, odour responses do not uniformly habituate across the experiment. Top, cartoon depiction of procedure for determining change in response amplitude over the course of the experiment for a single cell odour pair. Middle and bottom, pooled data for all cell–odour pairs, sorted by layer. Red lines correspond to distribution means (clustered odour set). **f**, Lifetime sparseness distributions (used to quantify tuning breadth) (Methods) in L2 and L3 across all experiments (1 = perfectly odour selective, 0 = completely non-selective, $^*P < 0.01$, permutation test on layer label). Distributions are built using all responsive neurons (significant response to at least one odour by auROC analysis) pooled by layer across all experiments (here and throughout, global: $n = 3$ mice, L2 = 854 neurons, L3 = 616 neurons; clustered: $n = 3$ mice, L2 = 867 neurons, L3 = 488 neurons; tiled: $n = 3$ mice, L2 = 427 neurons, L3 = 334 neurons). **g**, Population sparseness distributions (used to quantify response density) (Methods) in L2 and L3 (1 = few neurons active overall, 0 = all neurons active overall to an equal level). $^*P < 0.01$, permutation test on layer label. **h**, Probability density distributions of coefficient of variation for all significant cell-odour pairs identified with auROC analysis. $^*P < 0.01$, permutation test on layer label. **i**, Probability density distributions of ensemble correlations (that is, pairwise correlations between odour-evoked ensembles) between trial-averaged population odour responses in L2 (left) and L3 (middle). Dashed control curves indicate the distribution of ensemble correlations after shuffling odour labels independently across neurons. Ensemble correlations were determined independently for each mouse, and subsequently pooled. $^*P < 0.01$, permutation test on odour label. L3 exhibits greater correlations at the population level than L2 (right). $^*P < 0.01$, permutation test on layer label.

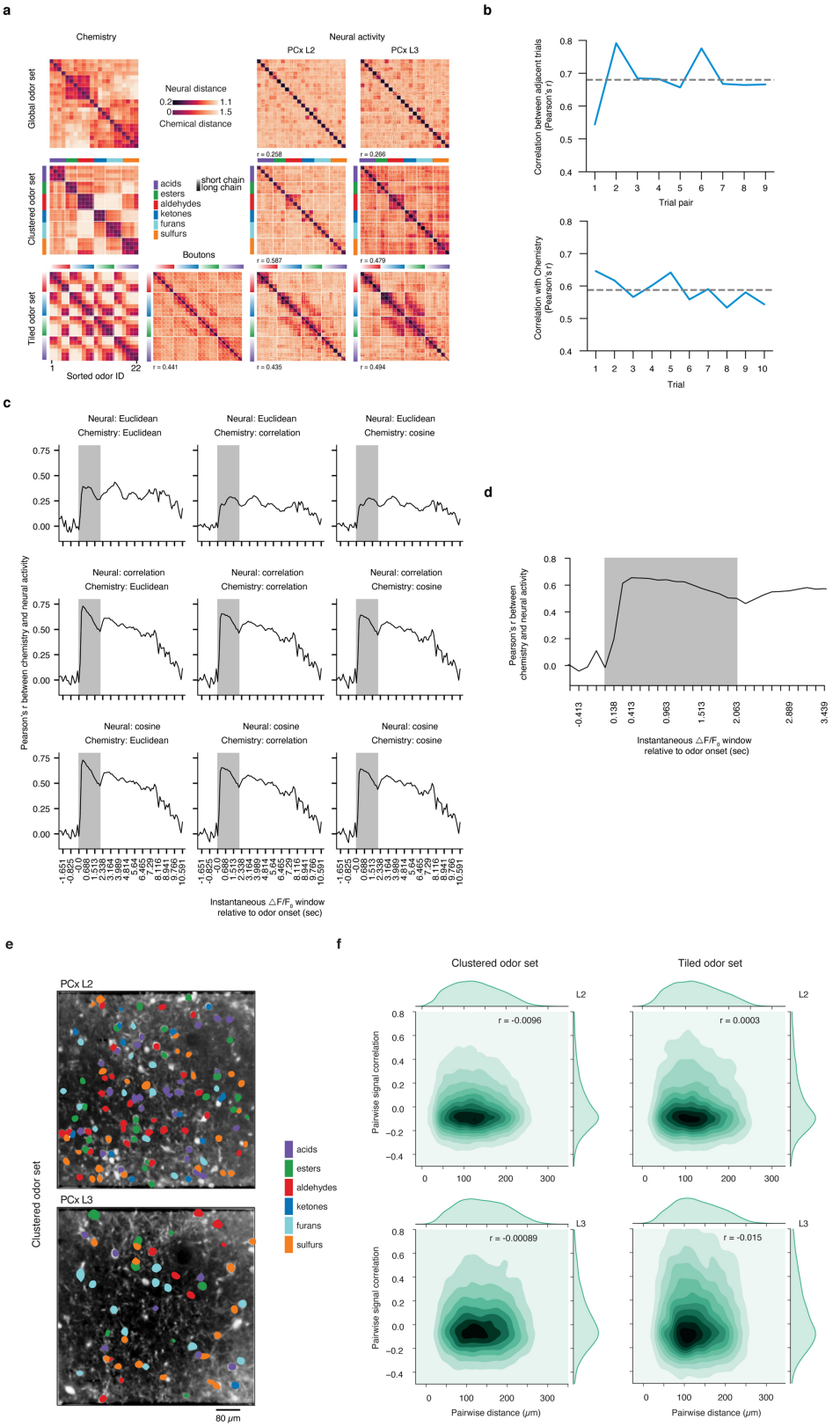


**Extended Data Fig. 4** | See next page for caption.

**Extended Data Fig. 4 | Cortical odour representations are stable from trial to trial and not chemotopically organized. a**, Left, pairwise odour chemical correlation matrices for the global, clustered and tiled odour sets. Rows and columns are sorted according to the chemical similarity between odours as assessed by hierarchical clustering (Methods). Middle and right, Pairwise correlation distances of single-trial, population representations for odours in the global, clustered, and tiled odour experiments in PCx L2 and L3 (and boutons for the tiled odour set). Rows and columns are sorted according to the chemical similarity between odours as on the left. Chemical colour code (*x* and *y* axis labels of matrices, indicating functional group associated with each group of molecules) is shown in the legend. *R* values indicate Pearson's correlation to odour chemistry. **b**, Top, structured odour relationships persist from trial to trial over the course of the experiment. Blue line represents the similarity of two correlation distance matrices built from population responses obtained on consecutive trials. Grey dashed line indicates mean across all trial-pair comparisons (10 trials, 9 trial pairs; clustered odour set, L3). Bottom, chemistry-based odour relationships correspond to matched cortical relationships obtained on a trial-by-trial basis. Dashed grey line represents the similarity of chemical and neural activity distances on a trial-by-trial basis. **c**, Correspondence between odour structure in PCx L3 (clustered odour set) and odour chemistry using three different distance metrics (correlation distances, Euclidean distances and cosine distances). Distance matrices calculated from population activity are obtained using instantaneous $\Delta F/F_0$ over 130 ms increments ($F_0$: baseline fluorescence averaged over a 1-s sliding window). Vertical lines delimit the 2-s odour presentation. **d**, Odour chemical relationships emerge within a few hundred milliseconds after odour onset and persist for several seconds after odour offset (see Extended Data Fig. 1e for associated PID traces). **e**, Example PCx L2 and L3 FOVs from a single mouse with each responsive neuron coloured according to its preferred odour in the clustered odour set. Neurons preferring odours belonging to different classes (legend) appear spatially intermingled in both L2 and L3. **f**, Contour plots of pairwise signal correlations, plotted with respect to distance in L2 and L3 for the clustered and tiled experiments. Darker colours indicate increased density (see margin distributions). Pearson's *r* is overlaid and indicates no spatial organization of odour representations in PCx.

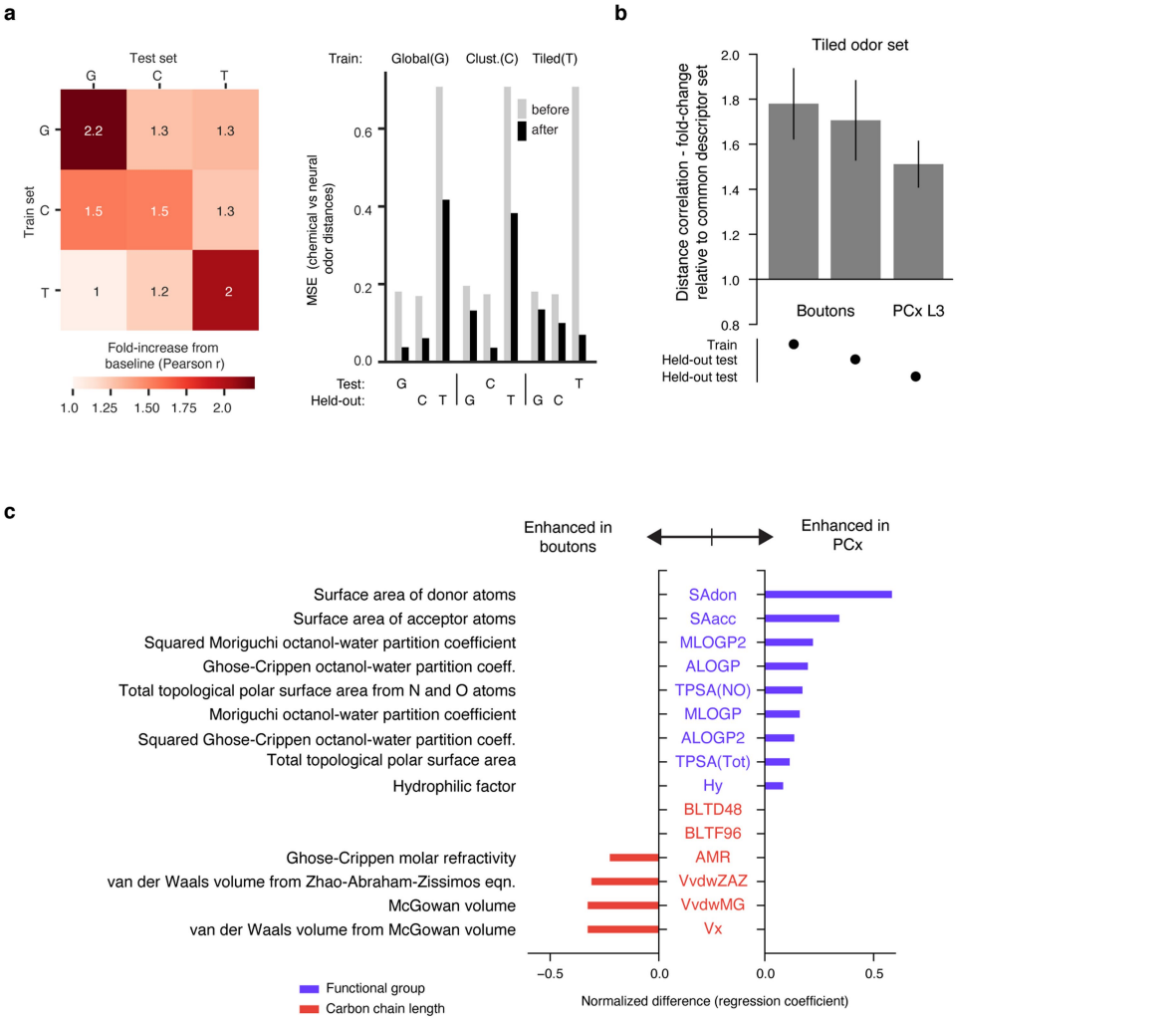


**Extended Data Fig. 5 | Lasso optimization identifies parsimonious sets of chemical descriptors that predict neural odour relationships. a**, Left, descriptors identified through training on one odour set also improve Pearson's correlation (*r*) between corresponding chemical and neural distances for held-out sets of odours. C, clustered; G, global; T, tiled. A value of 1 in the matrix corresponds to no improvement from baseline Pearson's *r* value after optimization. Baseline chemical-neural correlation is 0.22 for global; 0.48 for clustered; 0.37 for tiled (see Supplementary Table 1 for optimal descriptor sets). Right, reduction in mean-squared error (MSE) between chemical and neural odour pair distances for held-out odour sets (indicated below the *x* axis) after training on a single odour set (indicated above). Note that the five odours in common between the global and clustered odour sets (names in bold in Extended Data Fig. 2e) were discarded when evaluating performance on held-out data. The chemical features learned from the tiled odour set improved chemical–neural Pearson's correlations in the clustered odour experiment but not the global odour experiment, consistent with the odours belonging to the tiled set covering only a limited region of chemical odour space (left). However, despite the limited chemical overlap between the tiled and global odour sets, training on the tiled odour set still improved the correspondence between odour chemistry and neural responses for the global odour set as assessed by a reduction in the mean-squared error (right). **b**, Identifying a subset of chemical descriptors (from the original superset used to define odour space) using Lasso optimization on odour distances improves the correspondence to cortical activity (Methods, Supplementary Table 1). Training data were derived from the bouton dataset, and testing was performed for bouton responses to held-out odours within the tiled odour set, and also to cortical responses of the tiled odour set. Data are mean ± s.e.m. over cross-validation folds. **c**, The same procedure as in **b** was performed on a limited subset of 15 semantically relevant descriptors that comprise the 'molecular properties' block of the Dragon database; these descriptors include metrics that reflect molecular properties associated with functional groups (for example, donor or acceptor atom surface area), molecular weight (for example, van der Waals molecular volume) or a combination of both, such as 'hydrophilic factor', and reflect the main axes of diversity in the tiled odour set. Most descriptors enriched in the olfactory bulb covary with molecular weight (red descriptors). Most descriptors enriched in PCx reflect the combined presence of a charged atom and variable number of carbon atoms along the aliphatic series of the tiled odour set (blue descriptors). Note that these descriptors differ from those identified when querying the entire Dragon set using Lasso optimization (Supplementary Table 1), as this limited set of targeted descriptors (selected because their semantic meaning is transparent) may not afford optimal predictions over neural data.

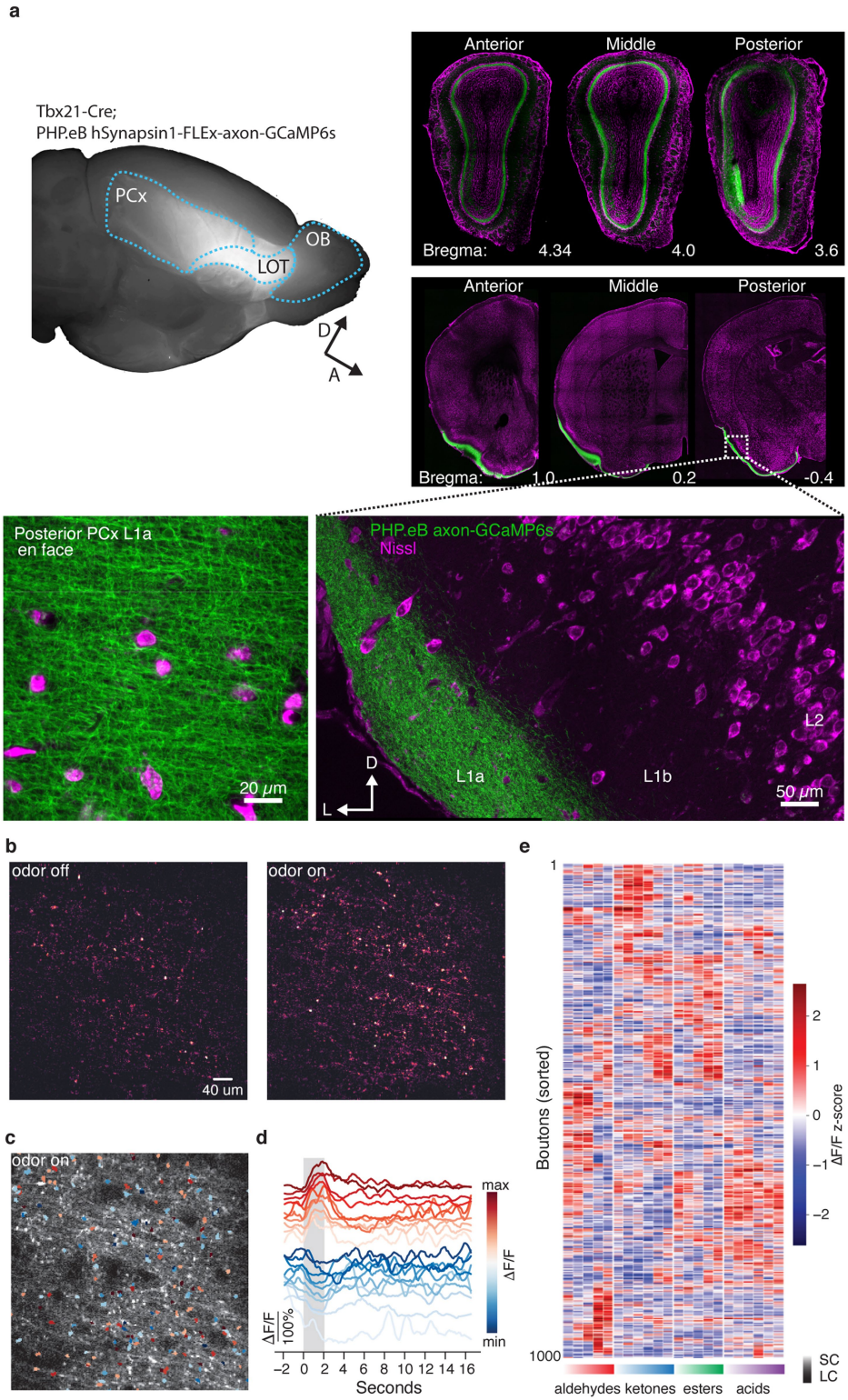


**Extended Data Fig. 6** | See next page for caption.

**Extended Data Fig. 6 | Functional imaging of OB axons in PCx via axonally targeted GCaMP6s. a**, Left, whole-mount depicting Tbx21-Cre-dependent expression of AAV PHP.eB hSynapsin1-FLEX-axon-GCaMP6s in OB projection neuron axons. GCaMP6s fluorescence is broadly distributed across piriform cortex. Right, coronal sections depicting GCaMP6s signal (green) in the mitral cell layer across the entire anterior-posterior extent of the olfactory bulb and cortex. Inset, bottom, GCaMP6s-labelled axons shown coursing through PCx L1a. Bottom left, en face image of L1a depicts dense and uniform distribution of axonal boutons. **b**, Difference heat map of a typical field-of-view (FOV) depicting baseline and odour-driven fluctuations in GCaMP6s signal. The strongest activation (light colour) is associated with axonal boutons. **c**, Time-averaged fluorescence signal of FOV in **b**. Overlay shows segmented ROIs corresponding to axonal boutons depicting increases (red) or decreases (blue) in fluorescence, averaged over multiple presentations of a single odour from the tiled odour set. **d**, Example average fluorescence from several boutons in **a**. Grey bar indicates odour delivery period, scale bar indicates response amplitude. For clarity, fluorescence time courses for each example bouton are offset along the *y* axis. **e**, Example bouton responses for the tiled odour set. Each row represents the trial-averaged response of a single bouton for two seconds during and after odour exposure (columns) depicted as *z*-scored $\Delta F/F_0$; rows are sorted hierarchically using correlation distance and average linkage. The functional group and carbon chain-length associated with each odour are indicated below each column; light-to-saturated gradient indicates progression from short-chain to long-chain odours. Note that, as has been observed previously for OB projection neurons, boutons exhibit a substantial amount of odour-driven suppression.

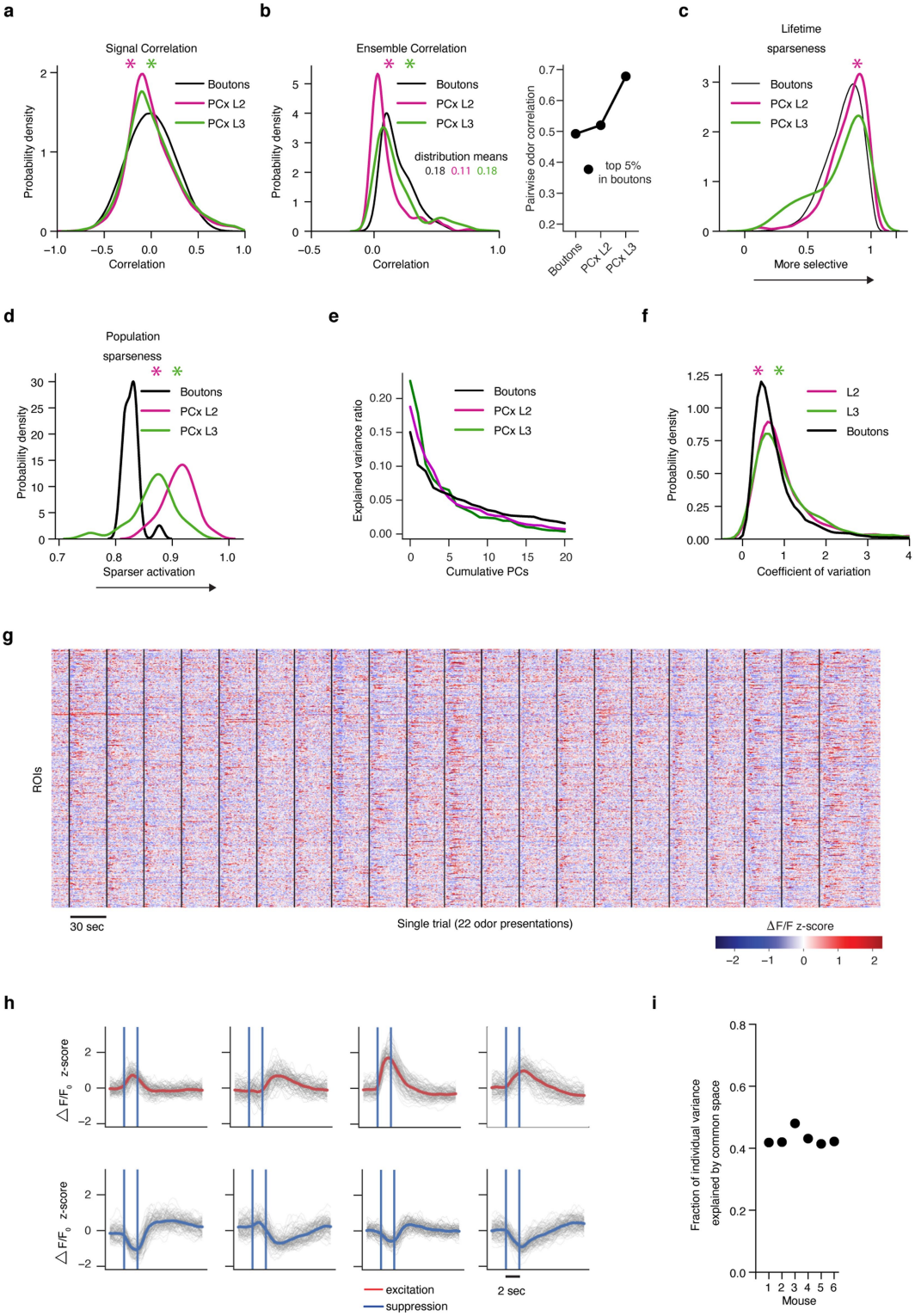


**Extended Data Fig. 7** | See next page for caption.

**Extended Data Fig. 7 | Bouton odour response properties. a**, Probability density distributions for boutons, PCx L2, and PCx L3 for signal correlations. **b**, Left, as in **a**, but for ensemble correlations. Right, for the top 5% most similar odour pairs identified in boutons, correlation for the same odour pairs in PCx. Ensemble responses in both PCx L2 and PCx L3 exhibit stronger similarity than boutons. **c**, **d**, Probability density distributions for boutons, PCx L2 and PCx L3, for lifetime and population sparseness. **e**, Cumulative neural variance explained with increasing numbers of principal components, indicating relatively higher dimensionality in boutons compared to PCx (that is, more uniform distribution of variance across principal components). **f**, Probability density distributions for boutons, PCx L2 and PCx L3 for coefficient of variation representing trial-to-trial response variability across cell–odour pairs. These data demonstrate that observed odour responses in boutons are more reliable than similar responses in the cortex. For **a**–**f**, only the tiled odour set is used. For lifetime sparseness, 1 = perfectly odour selective, 0 = completely non-selective. For population sparseness, 1 = few neurons responsive, 0 = all neurons equally responsive. Distributions are built using all responsive neurons/boutons (significant response to at least one odour by auROC analysis; boutons: 3160 ROIs across 6 subjects, PCx L2: 427 neurons across 3 subjects. PCx L3: 334 neurons across 3 subjects). Asterisk indicates significant difference between boutons and either L2 or L3: **a**, vs L2 $P < 10^{-27}$; vs L3 $P = 0.02$; **b**, vs L2 $P < 10^{-20}$; vs L3 $P < 0.005$; **c**, vs L2 $P < 10^{-9}$; vs L3 $P = 0.93$; **d**, vs L2 $P < 10^{-7}$ vs L3 $P < 10^{-4}$; **f**, vs L2: $P < 10^{-20}$; vs L3: $P < 10^{-23}$; two-sided Wilcoxon rank sum test for all comparisons. **g**, Single-trial $Z$-scored $\Delta F/F_0$ for 1,000 boutons recorded in PCx L1a during presentation of 22 odours belonging to the tiled odour set indicated by black lines. Redder colours indicating excitatory transients, and bluer colours indicate odour-evoked suppression. **h**, Response types observed in boutons (tiled odour set). Individual panels correspond to clusters identified using a Gaussian mixture model (Methods). Grey traces correspond to trial-averaged bouton-odour pairs. Coloured overlays represent mean response time course associated with each cluster. Blue vertical lines mark periods of odour presentation. **i**, Fraction of total odour-driven bouton variance in each individual mouse that can be attributed to the shared across-mouse structure as quantified by distance covariance analysis (Methods).

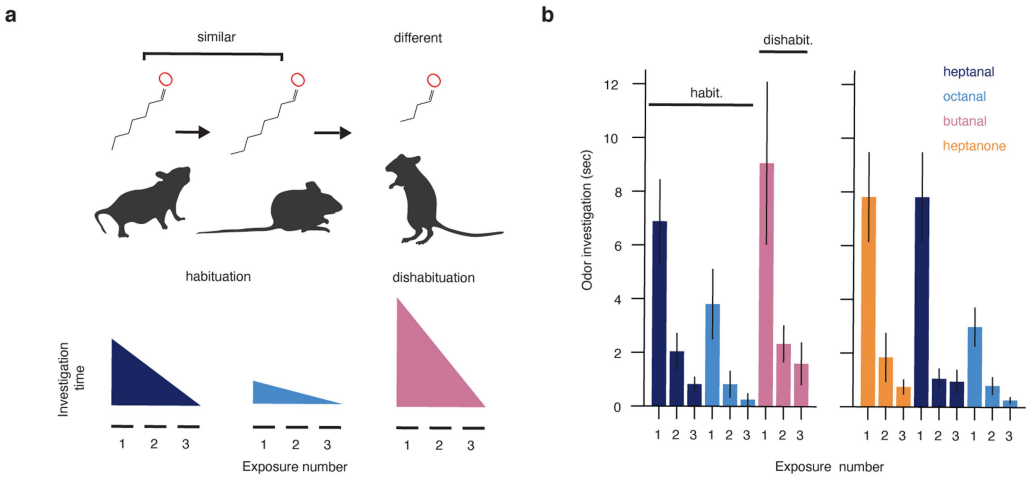


**Extended Data Fig. 8 | Habituation-dishabituation test for assessing perceptual similarity of odour pairs. a**, Left, mice presented with new odours exhibit investigation that diminishes over several consecutive presentations of the same odorant. Subsequent presentation of a perceptually different odour reinstates investigation, and presentation of a similar odour has little effect. The extent to which two odorants are perceptually related is assessed by the magnitude of rekindled interest in the second odour after habituation has occurred to the first. **b**, Investigation times for two different odour triplets. Data are mean ± s.e.m. ($n = 7$ and $n = 8$ mice, respectively). After habituation to heptanal, investigation of the closely related octanal (1-carbon difference) only modestly increases. Presentation of butanal after habituation to octanal (4-carbon difference) induces greater investigation. For the second triplet, presentation of heptanal after habituation to heptanone (0-carbon difference, different functional group) induces greater investigation, whereas subsequent presentation of octanal after habituation to heptanal (1-carbon difference, same functional group) induces much less investigation.

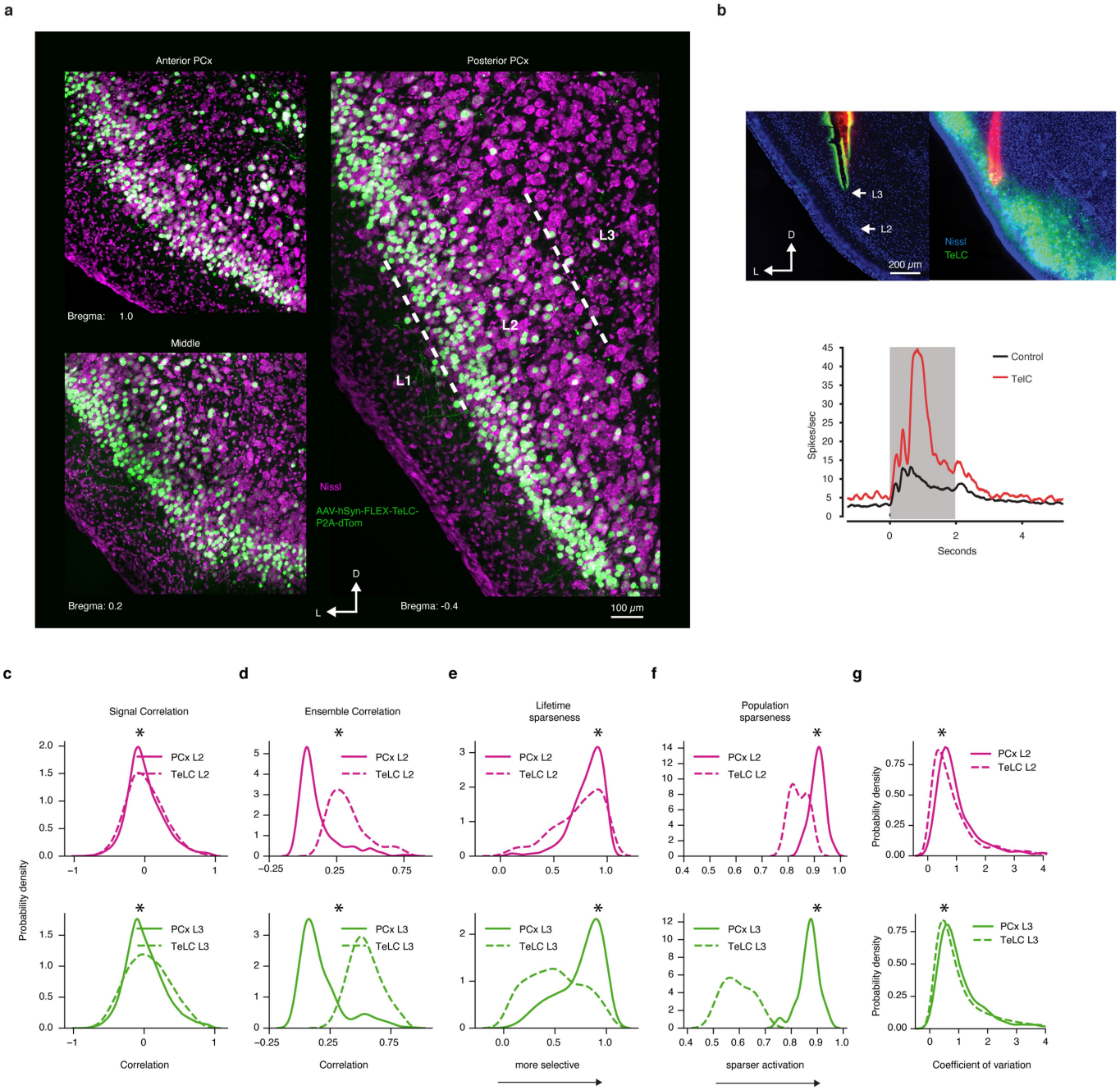


**Extended Data Fig. 9 | Inhibition of the associative network through cell-autonomous expression of tetanus toxin light chain in excitatory PCx neurons. a**, Uniform infection of excitatory pyramidal neurons in PCx L2 and L3 with AAV-hSyn-FLEX-TeLC-P2A-NLS-dTom in an Emx1-Cre mouse. **b**, Left, coronal section through PCx indicating placement of recording electrode. Right, single-unit odour-evoked activity (grand-average of all excitatory responses deemed as significant by auROC analysis) in Emx1-Cre mice expressing TeLC or wild-type controls. Disruption of cortical recurrent excitation enhances odour-evoked excitation, consistent with disruption of feedback inhibition. Grey bar indicates odour presentation ($n = 121$ cell–odour pairs from two Emx1-Cre mice expressing TeLC; $n = 229$ cell–odour pairs from four mice). **c**–**g**, Probability density distributions for the TeLC experiment for signal and ensemble correlations, lifetime and population sparseness, and coefficient of variation (constructed as in Extended Data Fig. 7, here only for the tiled odour set). For lifetime sparseness, 1 = perfectly odour selective, 0 = completely non-selective. For population sparseness, 1 = few neurons responsive, 0 = all neurons equally responsive. Distributions are built using all responsive neurons (significant response to at least one odour by auROC analysis; TeLC L2: 435 neurons across 3 subjects. TeLC L3: 590 neurons across 3 subjects. PCx L2: 427 neurons across 3 subjects. PCx L3: 334 neurons across 3 subjects). Asterisk indicates TeLC is significantly different from PCx L2 or L3: **c**, L2 $P < 10^{-8}$; L3 $P < 10^{-198}$; **d**, L2 $P < 10^{-46}$; L3 $P < 10^{-55}$; **e**, L2 $P < 10^{-05}$; L3 $P < 10^{-37}$; **f**, L2 $P < 10^{-7}$ L3 $P < 10^{-8}$; **g**, L2: $P < 10^{-10}$; L3: $P < 10^{-4}$; two-sided Wilcoxon rank sum test for all comparisons.

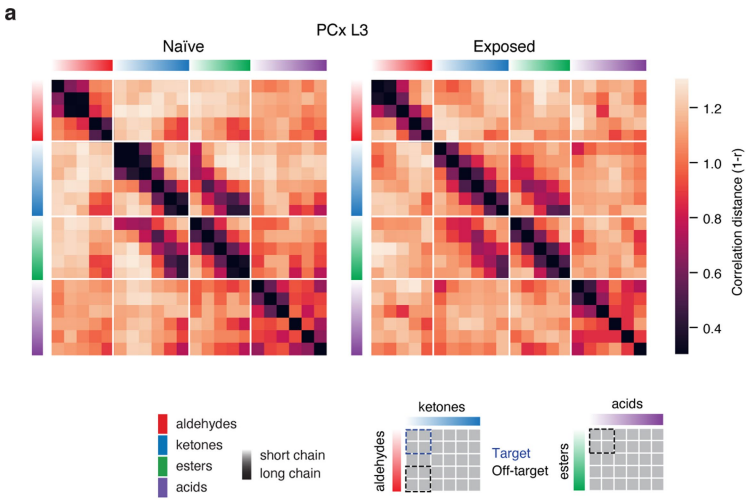


**Extended Data Fig. 10 | Passive odour experience modifies odour relationships. a**, Correlation distance matrices for the tiled odour set obtained from odour-naive (same data as in Figs. 1–4) mice as well as mice passively exposed to a target mixture of two short-chain aldehydes and two short-chain ketones in the home cage (Methods, Fig. 4e, f). Passive experience with the mixture increases odour similarity specifically between mixture components (target comparisons indicated in the legend in blue), but not between target ketones and long-chain aldehydes or short-chain esters and short-chain acids with which mice had no previous experience (off-target comparisons indicated in legend in black, nave: 334 neurons, $n = 3$ mice; exposed: 742 neurons, $n = 3$ mice).

nature research

Corresponding author(s): Sandeep R. Datta

# Reporting Summary

Nature Research wishes to improve the reproducibility of the work that we publish. This form provides structure for consistency and transparency in reporting. For further information on Nature Research policies, see Authors & Referees and the Editorial Policy Checklist.

## Statistical parameters

When statistical analyses are reported, confirm that the following items are present in the relevant location (e.g. figure legend, table legend, main text, or Methods section).

| n/a | Confirmed | |
|---|---|---|
| ☐ | ☒ | The exact sample size (*n*) for each experimental group/condition, given as a discrete number and unit of measurement |
| ☐ | ☒ | An indication of whether measurements were taken from distinct samples or whether the same sample was measured repeatedly |
| ☐ | ☒ | The statistical test(s) used AND whether they are one- or two-sided<br>*Only common tests should be described solely by name; describe more complex techniques in the Methods section.* |
| ☒ | ☐ | A description of all covariates tested |
| ☐ | ☒ | A description of any assumptions or corrections, such as tests of normality and adjustment for multiple comparisons |
| ☐ | ☒ | A full description of the statistics including central tendency (e.g. means) or other basic estimates (e.g. regression coefficient) AND variation (e.g. standard deviation) or associated estimates of uncertainty (e.g. confidence intervals) |
| ☐ | ☒ | For null hypothesis testing, the test statistic (e.g. *F*, *t*, *r*) with confidence intervals, effect sizes, degrees of freedom and *P* value noted<br>*Give P values as exact values whenever suitable.* |
| ☒ | ☐ | For Bayesian analysis, information on the choice of priors and Markov chain Monte Carlo settings |
| ☒ | ☐ | For hierarchical and complex designs, identification of the appropriate level for tests and full reporting of outcomes |
| ☐ | ☒ | Estimates of effect sizes (e.g. Cohen's *d*, Pearson's *r*), indicating how they were calculated |
| ☐ | ☒ | Clearly defined error bars<br>*State explicitly what error bars represent (e.g. SD, SE, CI)* |

*Our web collection on statistics for biologists may be useful.*

## Software and code

Policy information about availability of computer code

| | |
|---|---|
| Data collection | Imaging data was acquired using Scanimage 5 by Vidrio. Extraction of cell fluorescence was performed using the open-source software Suite2p. The odor library used for designing stimulus sets was obtained from www.thegoodscentscompany.com. Physicohemical descriptors were calculated using Dragon 7.0, KODE Inc. |
| Data analysis | Standard analyses were performed in Matlab and Python. The package "Pyrcca" (https://github.com/gallantlab/pyrcca) was used for multi-set canonical correlation analysis. Simulated annealing was performed using the open-source package simanneal 0.4.2 (https://pypi.org/project/simanneal/). |

For manuscripts utilizing custom algorithms or software that are central to the research but not yet described in published literature, software must be made available to editors/reviewers upon request. We strongly encourage code deposition in a community repository (e.g. GitHub). See the Nature Research guidelines for submitting code & software for further information.

## Data

Policy information about availability of data

All manuscripts must include a data availability statement. This statement should provide the following information, where applicable:

- Accession codes, unique identifiers, or web links for publicly available datasets
- A list of figures that have associated raw data
- A description of any restrictions on data availability

The data that support the findings of this study are available from the corresponding author upon reasonable request.

# Field-specific reporting

Please select the best fit for your research. If you are not sure, read the appropriate sections before making your selection.

☒ Life sciences ☐ Behavioural & social sciences ☐ Ecological, evolutionary & environmental sciences

For a reference copy of the document with all sections, see nature.com/authors/policies/ReportingSummary-flat.pdf

# Life sciences study design

All studies must disclose on these points even when the disclosure is negative.

| | |
|---|---|
| Sample size | Data collected from 18 animals was included in the study: each of three odor sets described in the study was presented to three animals such that each animal was exposed once to a single odor set for piriform imaging, the tiled odor set was presented to 3 additional mice for cortical imaging in the TeLC experiment, and six additional mice for the bouton imaging experiment. We found that due to the consistency in the structure of odor representations apparent across individuals, three animals sufficed for each condition. |
| Data exclusions | Data exclusion criteria are described in the Methods. Briefly, exclusion criteria were pre-established to select for experiments where imaging volumes spanning both Piriform cortical layers 2 and 3 (or in the case of the bouton experiment, Layer 1a) could be imaged continuously for at least 2.5 hours with minimal drift and motion artifacts, where a sufficient fraction of cortical neurons was labeled with GcAMP6s and where odor-evoked activity could be detected over the course of the entire imaging session. |
| Replication | The principal findings in this study were present in each individual and are reported in the main text. |
| Randomization | Not relevant. Animals were not assigned to different conditions based on whether they originated from the same breeding, litter, or housing cage, as all mice were derived from different cages and different breedings. In addition, the consistency in the structure of odor representations described in this study suggests that the observations are robust to these variables. |
| Blinding | Not relevant. The main findings in this study are not contingent on blind comparison of two or more experimental conditions, except for the scoring of the behavioral experiment, which was carried out in a blinded fashion. |

# Reporting for specific materials, systems and methods

### Materials & experimental systems

| n/a | Involved in the study |
|---|---|
| ☒ | ☐ Unique biological materials |
| ☒ | ☐ Antibodies |
| ☒ | ☐ Eukaryotic cell lines |
| ☒ | ☐ Palaeontology |
| ☐ | ☒ Animals and other organisms |
| ☒ | ☐ Human research participants |

### Methods

| n/a | Involved in the study |
|---|---|
| ☒ | ☐ ChIP-seq |
| ☒ | ☐ Flow cytometry |
| ☒ | ☐ MRI-based neuroimaging |

## Animals and other organisms

Policy information about studies involving animals; ARRIVE guidelines recommended for reporting animal research

| | |
|---|---|
| Laboratory animals | Male 8-16 week old C57/BL6J mice; for cortical imaging, mice harboring the Vgat-ires-Cre (Jackson Stock No. 028862) and ROSA26-LSL-TdTomato reporter alleles (Jackson Stock No. 007914) were used, and for bulb imaging, mice harboring the Tbet-Cre |

allele (Jackson Stock 024507) were used.

Wild animals

This study did not involve the use of wild animals.

Field-collected samples

This study did not involve samples collected from the field.